CHAPTER 3

THERMODYNAMICS OF PROTON AND ELECTRON TRANSFER IN TETRANUCLEAR CLUSTERS WITH MN–OH_2/OH MOTIFS RELEVANT TO H_2O ACTIVATION BY THE OXYGEN EVOLVING COMPLEX IN PHOTOSYSTEM II

The text for this chapter was reproduced in part from:

Reed, C. J.; Agapie, T. *J. Am. Chem. Soc.*, **2018**, *140*, 10900 – 10908

ABSTRACT

We report the synthesis of site-differentiated heterometallic clusters with three Fe centers and a single Mn site that binds water and hydroxide in multiple cluster oxidation states. Deprotonation of [$Fe^{III/II}_3Mn^{II}$–OH_2] clusters leads to internal redox reorganization resulting in formal oxidation at Mn to generate [$Fe^{III/II}_3Mn^{III}$–OH]. ^{57}Fe Mössbauer spectroscopy reveals that oxidation state changes (three for [$Fe^{III/II}_3Mn^{II}$–OH_2] and four for [$Fe^{III/II}_3Mn^{III}$–OH] clusters) occur exclusively at the Fe centers; the Mn center is formally Mn^{II} when water is bound and Mn^{III} when hydroxide is bound. Experimentally determined pK_a (17.4) of the [$Fe^{III}_2Fe^{II}Mn^{II}$–OH_2] cluster and the reduction potentials of the [Fe_3Mn–OH_2] and [Fe_3Mn–OH] clusters were used to analyze the O–H bond dissociation enthalpies ($BDE_{O–H}$) for multiple cluster oxidation states. $BDE_{O–H}$ increases from 69, to 78, and 85 kcal/mol for the [$Fe^{III}Fe^{II}_2Mn^{II}$-OH_2], [$Fe^{III}_2Fe^{II}Mn^{II}$-OH_2], and [$Fe^{III}_3Mn^{II}$-OH_2] clusters, respectively. Further insight of the proton and electron transfer thermodynamics of the [Fe_3Mn–OH_x] system was obtained by constructing a potential–pK_a diagram; the shift in reduction potentials of the [Fe_3Mn–OH_x] clusters in the presence of different bases supports the $BDE_{O–H}$ values reported for the [Fe_3Mn–OH_2] clusters. A lower limit of the pK_a for the hydroxide ligand of the [Fe_3Mn–OH] clusters was estimated for two oxidation states. These data suggest $BDE_{O–H}$ values for the [$Fe^{III}_2Fe^{II}Mn^{III}$–OH] and [$Fe^{III}_3Mn^{III}$–OH] clusters are greater than 93 and 103 kcal/mol, which hints to the high reactivity expected of the resulting [Fe_3Mn=O] in this and related multinuclear systems.

INTRODUCTION

During photosynthesis, water oxidation is catalyzed at the active site of Photosystem II (PSII) by a [$CaMn_4O_5$] cluster known as the oxygen evolving complex (OEC).[1] The catalytic mechanism is outlined by the Kok cycle, with the cluster transitioning through five distinct so-called S-states (S_0, S_1, …, S_4).[2] Four sequential oxidations of the cluster occur ($S_0 \rightarrow \rightarrow S_4$), followed by the O–O bond forming step, with concomitant loss of O_2 and binding of H_2O to complete the cycle ($S_4 \rightarrow S_0$). Protons are sequentially released from the active site during the S-state cycle; deprotonation of bound H_2O in this stepwise manner prevents the buildup of significant charge at the active site, facilitating the further oxidation of the [$CaMn_4O_5$] cluster.[3] PSII utilizes a nearby tyrosine radical (Y_z•) as a mediator to transfer electrons/protons away from the OEC during turnover; because of the nature of the tyrosine radical, proton-coupled electron transfer (PCET) of the H_2O-derived ligands bound to the OEC is considered to play an important role in the Kok cycle.[3-4] Due to the wealth of information available in X-ray crystallographic[1b-d, 5], EPR[6], and X-ray absorption[2b, 6d, 7] spectroscopic techniques, much is known about the Mn oxidation states and electronic environment of the OEC in the S_0 through S_3 states of the Kok cycle. More challenging has been understanding the precise protonation state of H_2O ligands and relevant neighboring amino acid residues of any S-state; computational studies of the OEC have considered a variety of possible protonation states.[4c, 8] Experimentally, time-resolved IR spectroscopy has been helpful in gaining insight to the dynamics of protons at the active site during turnover.[6j, 9] Furthermore, multiple computational models of the OEC mechanism invoke a terminal Mn-oxo as a crucial part of the O–O bond forming S_4 intermediate[2c, 10]. Therefore, there is significant interest in understanding the chemistry of a Mn–OH_2 species undergoing multiple proton and electron transfers to reach a reactive terminal Mn-oxo.

The chemistry of synthetic Mn-aquo, -hydroxo, and -oxo motifs has been a subject of interest for inorganic chemists, particularly within the context of gaining insight into the thermodynamic basis of Mn–OH_x PCET reactivity and how it relates to the mechanism of the OEC.[11, 12, 13] Reported mononuclear systems have been able to probe the roles of Mn oxidation state[12c, 12d, 12i], ligand field[11a, 11f, 13b], and oxygen ligand protonation state[11j, 12j] on PCET reactions and the intrinsic O–H bond dissociation enthalpies ($BDE_{O–H}$) of Mn–OH_x moieties. There are fewer examples of such studies with multinuclear Mn complexes, with most of the reports examining the PCET chemistry of bridging oxo moieties,[14] as opposed to terminally bound OH_x ligands.[15] Most of these reports are limited to binuclear Mn complexes or systems where only a single redox couple could be examined. The PCET reactivity of a synthetic $Mn^{III}_3Mn^{IV}O_3(OH)$ cubane cluster has been examined, where the $BDE_{O–H}$ of the μ_3-OH could be estimated to be >94 kcal/mol; however, precise determination of the thermodynamic bond strength was complicated by subsequent decomposition of the protonated cubane.[14d] A report of proton and electron transfer at a terminal Mn-OH_x moiety with an adjacent Mn center over three oxidation states (Mn^{III}_2, $Mn^{III}Mn^{IV}$, and Mn^{IV}_2) represents a very rare example of thermodynamic studies of a terminal Mn-OH_x in a multinuclear system.[15a] Access to a suitable synthetic platform to interrogate the effects of *multiple* neighboring redox-active metal centers on the chemistry of a terminal Mn–OH_x motif may facilitate a more complete picture of the dynamics of proton and electron transfer of the OEC leading up to its reactive S_4 state, and more generally lead to a better understanding of the behavior of metal clusters in reactions involving water, dioxygen, and multi-electron transformations.

Our group has demonstrated the utility of rationally-designed, well-defined molecular clusters for probing structure-function relationships in multinuclear first-row transition metal complexes, acting as models of complex active sites found in biology.[16, 17] Recently, we have

studied a family of tetranuclear Fe and Mn complexes composed of three coordinatively-saturated metal ions bridged to a fourth (apical) metal center through substituted pyrazolate (or imidazolate) ligands and a μ_4-single atom ligand.[18] The apical metal has a coordination site available for exogenous ligands, allowing for the study of substrate binding and reactivity by a molecular cluster. With bulky and nonpolar phenyl substituents in the 3 position of the pyrazolate ligands coordination of bulkier ligands remains inhibited, and intramolecular ligand activation had been observed.[18d-f] In contrast, previous group members, Drs. Zhiji Han and Kyle Horak, have established that amino-phenylpyrazolate ligands, which are more open and facilitate hydrogen bonding interactions, support oxo-bridged tetramanganese clusters bearing a Mn^{III}–OH moiety (Scheme 1; **[$LMn_3O(PzNHPh)_3Mn(OH)$][OTf]**), which are competent for catalyzing electrochemical water oxidation to H_2O_2.[19] Detailed examination of the PCET reactivity of this cluster was challenging, however, which may have been due, in part, to the acidity and possible redox non-innocence of the amino-phenylpyrazolate ligands. Other previous efforts within the Agapie group to examine PCET reactivity of clusters includes studies of related tri-iron-oxo/-hydroxo clusters bearing a pendant redox inactive metal, **[$LFe_3O_2M(OAc)_2(DME)(OTf)]^{n+}$** (Scheme 1), by Dr. Davide Lionetti.[20]

Scheme 1. Previous Multinuclear Complexes Studied by the Agapie Group for PCET Reactivity[19-20]

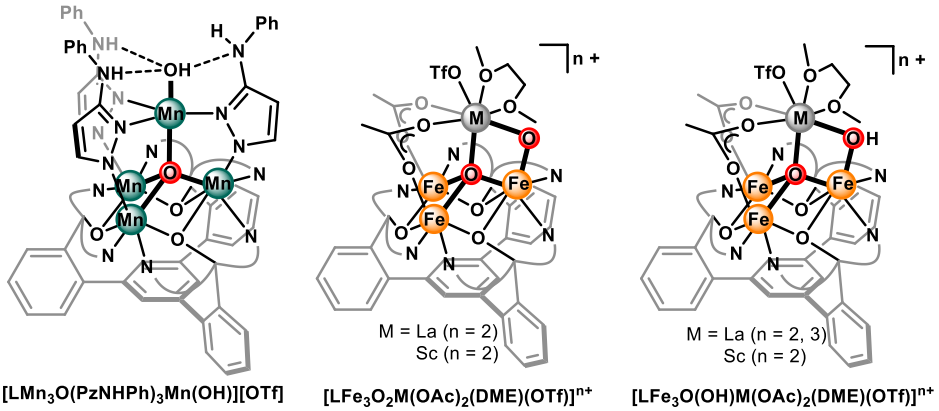

[$LMn_3O(PzNHPh)_3Mn(OH)$][OTf] [$LFe_3O_2M(OAc)_2(DME)(OTf)]^{n+}$ [$LFe_3O(OH)M(OAc)_2(DME)(OTf)]^{n+}$

Here, clusters with unsubstituted bridging pyrazolate ligands (Pz^-) were synthesized to further promote intermolecular reactivity between apical Mn–OH_x groups and external acids, bases, or hydrogen atom donors/acceptors. A heterometallic cluster composition, in this case [Fe_3Mn], was targeted to provide a spectroscopic handle of metal oxidation states within the cluster, via ^{57}Fe Mössbauer spectroscopy. The thermodynamic aspects of the PCET reactivity of these $LFe_3O(Pz)_3Mn(OH_x)^{n+}$ clusters were investigated through examination of the discrete electron and proton transfers taking place over multiple redox states. The results herein establish the significant influence redox changes at distal metal sites in a cluster have on a Mn–OH_x motif and, conversely, how this motif's protonation state can modulate the electron distribution between metals in the cluster.

RESULTS AND DISCUSSION

Synthesis and Characterization of Pyrazolate Bridged [Fe_3Mn] Clusters. The [$Fe^{III}_2Fe^{II}Mn^{II}$] cluster (**2-[OTf]**) can be prepared via one-pot synthesis, starting from previously reported **[LFe_3(OAc)(OTf)][OTf]** complex.[18a] Sequential addition of $Ca(OTf)_2$ (which serves to sequester the equivalent of acetate in the starting material, to avoid mixtures of counterions), potassium pyrazolate, iodosobenzene (PhIO), and manganese (II) trifluoromethanesulfonate bis-acetonitrile solvate ($Mn(OTf)_2$ • 2 MeCN) allows for isolation of the desired complex (Figure 1C). ^{1}H NMR and Mössbauer spectra of **2-[OTf]** are similar to our previously reported $[LFe_3O(PhPz)_3Mn][OTf]_2$ cluster which was synthesized using sodium phenyl pyrazolate, supporting the assignment that the apical metal is Mn (Figure 2).[18e] The structure of **2-[OTf]** was confirmed by single crystal X-ray diffraction (see Figure 1A for isostructural **1-[OTf]**); the cluster geometry is analogous to the substituted pyrazolate and imidizolate tetranuclear clusters, with a single μ_4-interstitital ligand and pyrazolates bridging

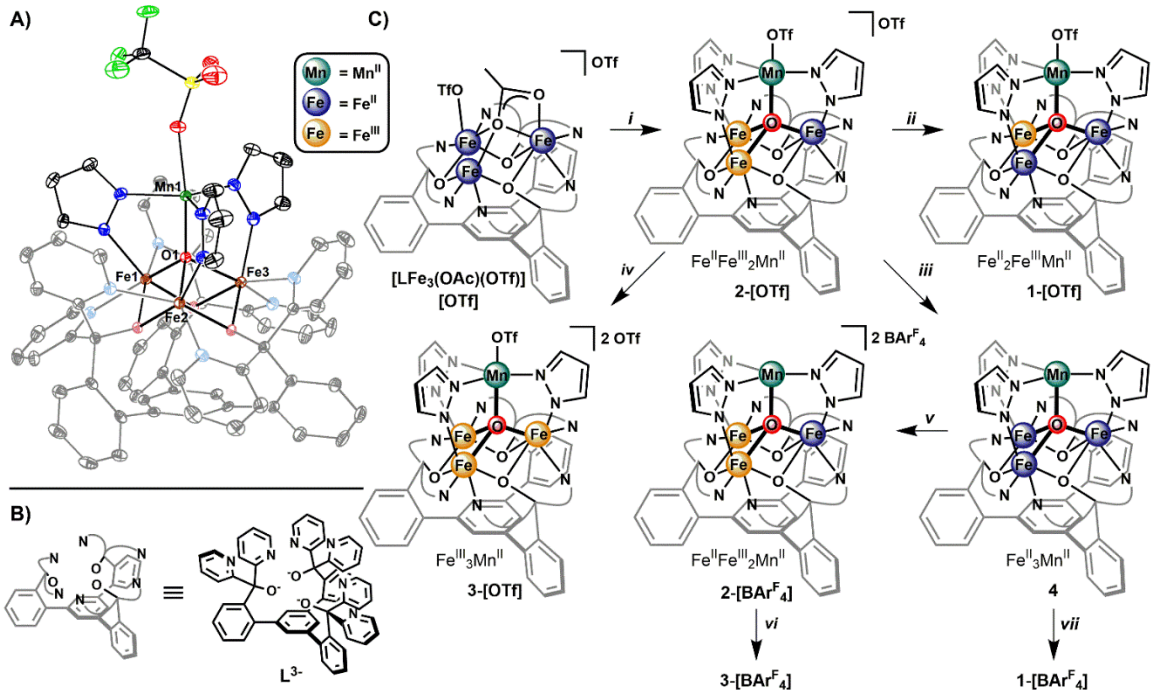

Figure 1. (A) Crystal structure of tetranuclear Fe_3Mn cluster **1-[OTf]** with ellipsoids shown at the 50% probability level. Solvent molecules, outer-sphere counterions, and H atoms are omitted for clarity. (B) 1,3,5-triarylbenzene ligand platform ($\mathbf{L^{3-}}$). (C) Synthetic scheme of Fe_3Mn clusters with triflate and $^{-}[BAr^{F}{}_4]$ counterions. Conditions: (i) One-pot synthesis in THF with (1) $Ca(OTf)_2$ (1 equiv., 60 min), (2) potassium pyrazolate (3.1 equiv., 20 min), (3) PhIO (1 equiv., 90 min), and (4) $Mn(OTf)_2 \bullet 2$ MeCN (1.3 equiv., 18 hr); (ii) $CoCp_2$ (1 equiv.), THF, 60 min; (iii) Na/Hg (2.6 equiv. Na), THF, 4 hr; (iv) AgOTf (1 equiv.), THF, 30 min; (v) $Ag[BAr^{F}{}_4] \bullet 2$ MeCN (2 equiv.), Et_2O, 15 min; (vi) $[^{Ac}Fc][BAr^{F}{}_4]$ (1 equiv.), THF, 10 min; (vii) $Ag[BAr^{F}{}_4] \bullet 2$ MeCN (1 equiv.), Et_2O, 15 min.

---

each Fe center of the tri-nuclear core to the apical Mn.[18] In the case of the previously reported clusters, the apical metal typically adopts a four-coordinate, trigonal pyramidal geometry since the sterics of the substituted pyrazolate ligands disfavor binding of one of the triflate counterions to the apical metal. Here, the apical Mn is ligated by one triflate counterion with

a trigonal bipyramidal geometry, indicative of the increased steric accessibility of the apical metal with the unsubstituted pyrazolates.

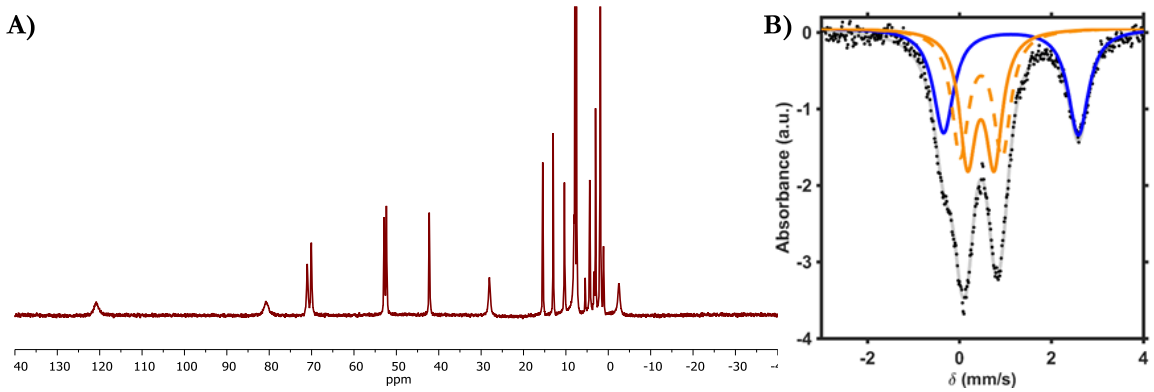

Figure 2. (A) ^{1}H NMR (300 MHz) of **2-[OTf]** in CD_3CN. (B) Zero applied field ^{57}Fe Mössbauer spectrum of **2-[OTf]** (black dots) fit with three equal quadrupole doublets (gray line) with parameters: (i) $\delta = 1.12$ mm/s, $|\Delta E_q| = 2.93$ mm/s (blue trace), (ii) $\delta = 0.47$ mm/s, $|\Delta E_q| = 0.58$ mm/s (solid orange trace), and (iii) $\delta = 0.42$ mm/s, $|\Delta E_q| = 0.91$ mm/s (dashed orange trace).

Cyclic voltammetry (CV) data of **2-[OTf]** in MeCN show a quasi-reversible oxidation at -0.11 V, a quasi-reversible reduction wave at -0.84 V, and an irreversible reductive process below -1.50 V (Figure 3; all potentials vs Fc/Fc^{+}). The one electron reduced (**1-[OTf]**), and one electron oxidized (**3-[OTf]**) clusters were prepared via chemical reduction/oxidation of **2-[OTf]** with cobaltocene ($CoCp_2$) and silver trifluoromethanesulfonate (AgOTf), respectively. The X-ray crystal structures of these three compounds all have identical coordination modes for the metal centers (Figure 1A). Bond distances between the metals and the μ_4-oxo are consistent with the redox processes taking place at the Fe centers, with the apical Mn maintaining a +2 oxidation state across the series **1-[OTf]** – **3-[OTf]** (Table 1). Mössbauer data corroborate these oxidation state assignments, and are similar to our previously characterized clusters.[18a-e]

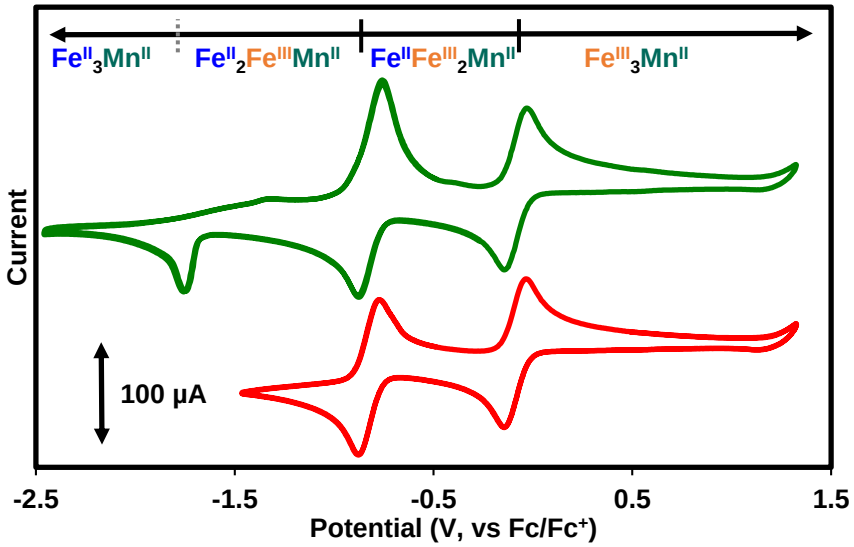

Figure 3. Cyclic voltammogram (green trace) of **2-[OTf]** (2.8 mM) in MeCN and 100 mM $[Bu_4N][PF_6]$ at a scan rate of 200 mV/s with glassy carbon, Pt-wire, and Ag-wire as working, counter, and reference electrode, respectively. The open circuit potential was -0.5 V. (Red trace) Partial CV of **2-[OTf]** of the quasi-reversible electrochemical features.

Table 1. Selected Bond Distances, ^{57}Fe Mössbauer Parameters, and Oxidation State Assignments for Structurally Characterized Compounds

Metal Center	M–μ_4-O1; (*Mn1–O2*) distance (Å)	δ (mm/s)	$\lvert\Delta E_q\rvert$ (mm/s)	Assignment
		1-[OTf]		
Fe1	1.912(2)	0.56	1.32	*h.s.* Fe^{III}
Fe2, Fe3	2.054(2), 2.112(2)	1.14, 1.13	3.51, 3.02	*h.s.* Fe^{II}
Mn1	1.997(2); (*2.249(2)*)			Mn^{II}
		2-[OTf]		
Fe1, Fe2	1.951(2), 1.966(2)	0.47, 0.42	0.58, 0.91	*h.s.* Fe^{III}
Fe3	2.097(2)	1.12	2.93	*h.s.* Fe^{II}
Mn1	2.053(2); (*2.167(3)*)			Mn^{II}
		2-[OTf] (H_2O)		
Fe1, Fe2	1.923(5), 1.984(5)			*h.s.* Fe^{III}
Fe3	2.092(5)			*h.s.* Fe^{II}
Mn1	2.064(5); (*2.163(6)*)			Mn^{II}
		3-[OTf]		
Fe1, Fe2, Fe3	1.980(4), 1.982(4), 1.989(4)	0.44	0.80	*h.s.* Fe^{III}
Mn1	2.107(4); (*2.162(5)*)			Mn^{II}
		6-[OTf]		
Fe1	2.003(7)	0.53	0.76	*h.s.* Fe^{III}
Fe2, Fe3	2.126(7), 2.051(7)	1.09, 1.08	3.09, 2.58	*h.s.* Fe^{II}
Mn1	1.838(8); (*1.843(9)*)			Mn^{III}

Preparation of Mn–OH_2 and Mn–OH Clusters. Binding of water to these clusters was investigated; however, the coordination of triflate to the apical Mn complicates direct access to the Mn–OH_2 moiety for all oxidation states of the cluster. The triflate ligand in **2-[OTf]** is sufficiently labile to allow for isolation of the Mn–OH_2 cluster as single crystals by slow diffusion of Et_2O into a MeCN/5% H_2O solution of the cluster, and its structure was confirmed via X-ray crystallography (**2-[OTf] (H_2O)**; Figure 4B). Attempts to obtain crystals of the analogous reduced Mn-OH_2 cluster (**1-[OTf] (H_2O)**) were unsuccessful; we postulate that the difficulty lies in poor crystallinity of the complex, as opposed to an inability to

coordinate H_2O over triflate. Crystallization attempts of **3-[OTf]** in MeCN/5% H_2O solutions produced crystals of triflate coordinated clusters, demonstrating the complication of preparing Mn–OH_2 clusters across these oxidation states with the triflate counterions. The structure of **2-[OTf] (H_2O)** displays H_2O coordinated to the apical Mn, with a long Mn–O distance of 2.163(6) Å, consistent with a Mn^{II}–OH_2 assignment;[13e, 21] furthermore, both triflate counterions are hydrogen bonding to each proton of the Mn–OH_2 moiety through one of the sulfonate oxygen atoms (O_{aquo}–O_{OTf} distances of 2.787 and 2.695 Å).

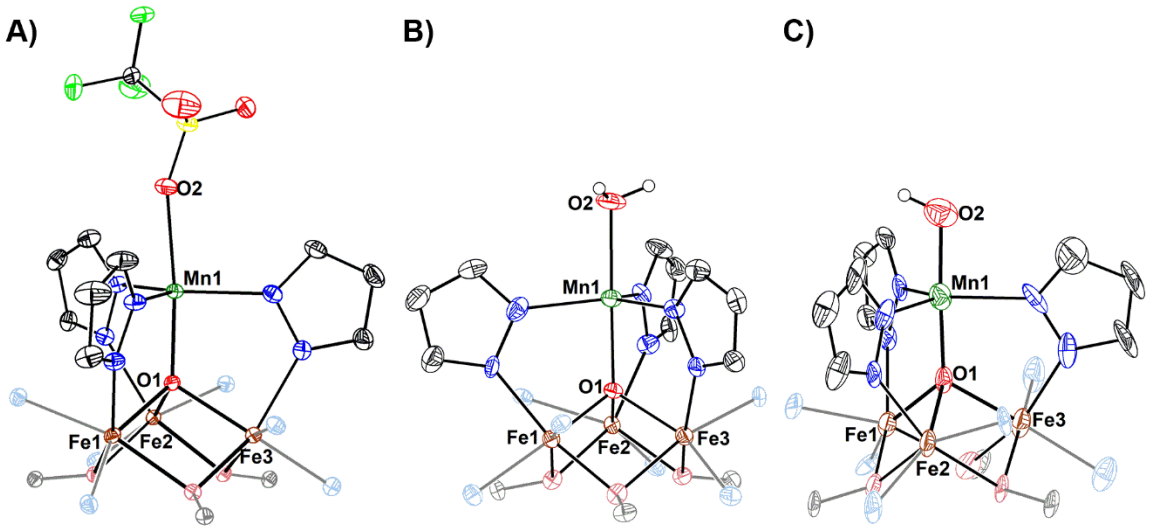

Figure 4. Truncated crystal structures of (A) **1-[OTf]**, (B) **2-[OTf] (H_2O)**, and (C) **6-[OTf]**. Ellipsoids are shown at the 50% probability level with solvent molecules, outersphere counterions, and hydrogen atoms (except for hydrogen atoms on O2) are omitted for clarity.

To ensure that H_2O remained coordinated to the cluster in solution, experiments were performed in THF, a less coordinating solvent than MeCN, and triflate counterions were replaced with the non-coordinating tetrakis[3,5-bis(trifluoromethyl)phenyl]borate ([$BAr^F{}_4$]) anion. This was accomplished by reducing the dicationic cluster, **2-[OTf]**, with Na/Hg amalgam in THF to obtain the neutral all M^{II} cluster, **4**, as a blue solid (Figure 1C). Similar to the related neutral phenyl pyrazolate clusters,[18a] **4** is either insoluble or unstable in most organic

solvents, so its chemistry towards H_2O was not pursued. Oxidation of **4** with 1 and 2 equiv of $Ag[BAr^F_4]$ • 2 MeCN affords **1-[BAr$^F_4$]** and **2-[BAr$^F_4$]**, respectively (Figure 1C). The $[Fe^{III}_3Mn^{II}]$ cluster, **3-[BAr$^F_4$]**, was prepared by oxidation of **2-[BAr$^F_4$]** with acetyl-ferrocenium ($[^{Ac}Fc][BAr^F_4]$). All these clusters are highly soluble in THF and bind H_2O under conditions where it is present in ~100 molar equivalents (Figures 5 - 7). Significant decomposition is observed when H_2O concentrations above ~1000 equivalents were used; therefore, all the studies described herein were performed on ca. 2 mM of a cluster with $^-[BAr^F_4]$ counterions in THF solution with 250 mM H_2O, as these conditions displayed ^{1}H NMR spectra consistent with complete or near complete binding of H_2O to the apical Mn.

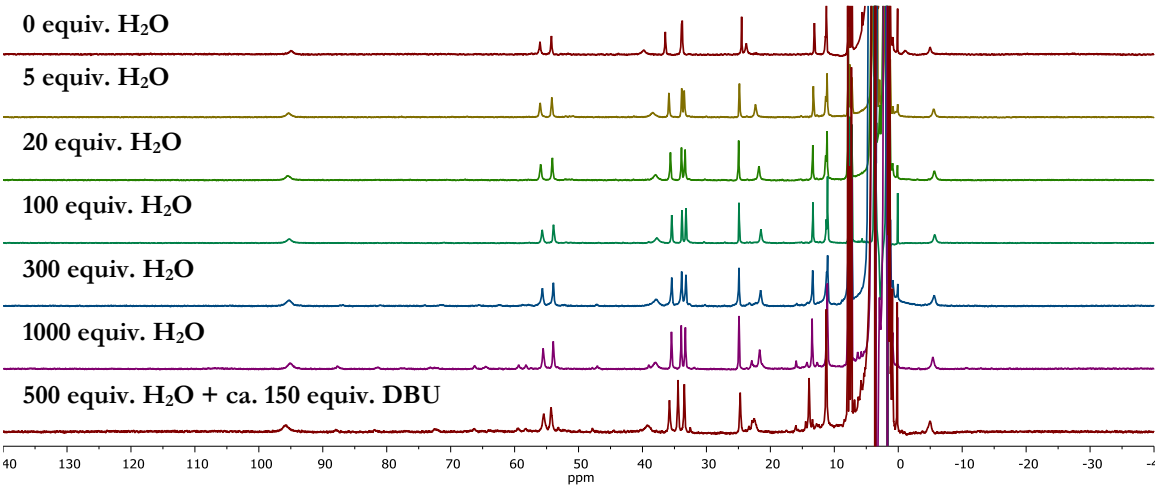

Figure 5. ^{1}H NMR spectra (500 MHz) of 2mM $[LFe_3O(Pz)_3Mn][BAr^F_4]$ (**1-[BAr$^F_4$]**) in THF/C_6D_6 with various equivalents of H_2O. Splitting of the peak at ~35 ppm was used to judge the amount of H_2O coordination, which appeared complete at > 20 equivalents H_2O. Addition of excess 1,8-diazabicyclo(5.4.0)undec-7-ene (DBU) leads to no significant change in the ^{1}H NMR spectrum.

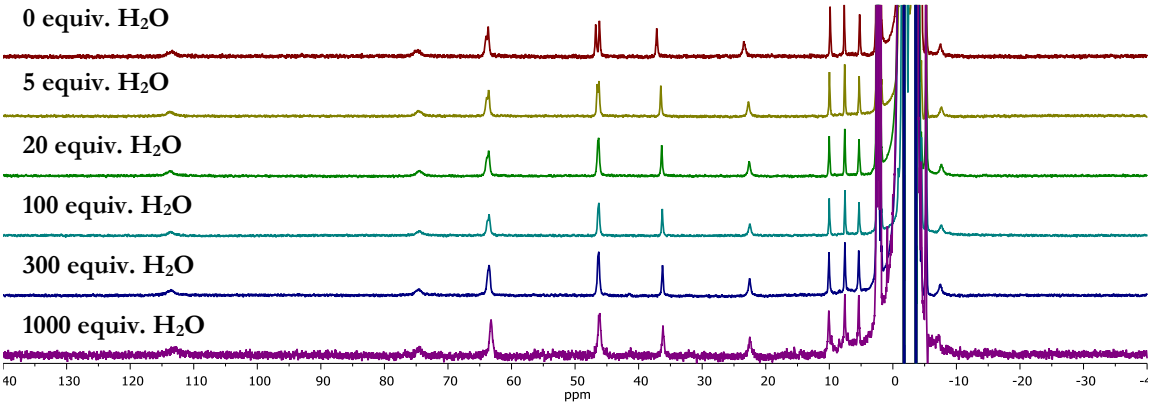

Figure 6. ^{1}H NMR spectra (500 MHz) of 2mM $[LFe_3O(Pz)_3Mn][BAr^F{}_4]_2$ (**2-[BAr$^F{}_4$]**) in THF/C_6D_6 with various equivalents of H_2O. Coalescence of the two peaks at ~45 ppm was used to judge the amount of H_2O coordination, which appeared complete at > 20 equivalents H_2O.

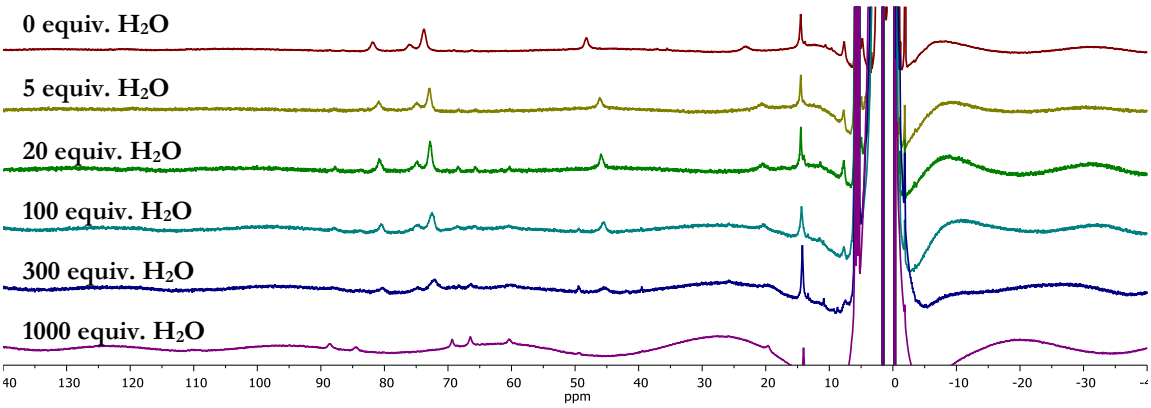

Figure 7. ^{1}H NMR spectra (500 MHz) of $[LFe_3O(Pz)_3Mn][BAr^F{}_4]_3$ (**3-[BAr$^F{}_4$]**) in THF/C_6D_6 with various equivalents of H_2O. The upfield shift of the peak at ~50 ppm was used to judge the amount of H_2O coordination, which appeared complete at > 20 equivalents H_2O.

Deprotonation of the Mn–OH_2 moiety in the $[Fe^{III}{}_2Fe^{II}Mn^{II}]$ cluster, **2-[BAr$^F{}_4$]**, was accomplished by addition of 1 equivalent of a relatively strong organic base, 1,8-diazabicyclo(5.4.0)undec-7-ene (DBU; pK_a(THF) = 19.1)[22], or by stirring a THF solution of **2-[BAr$^F{}_4$]** over solid KOH for 30 minutes. Both reactions lead to the same species based on the

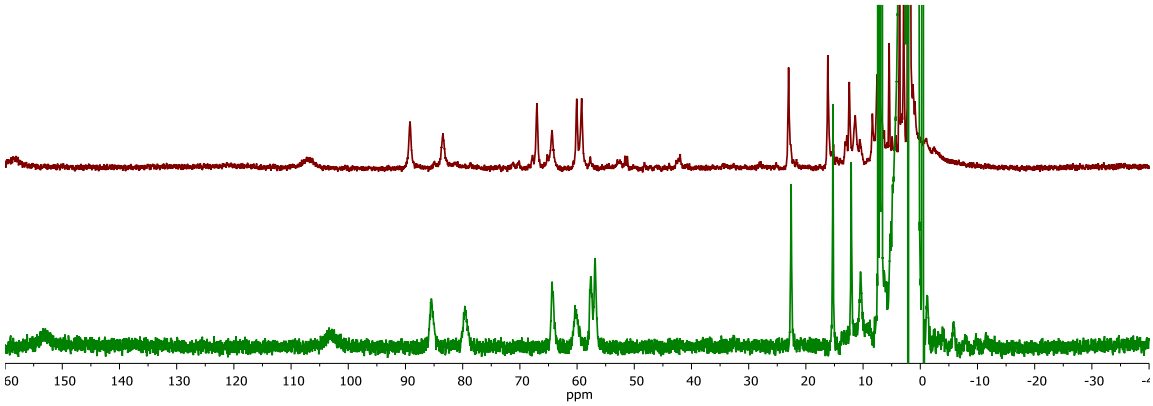

Figure 8. ^{1}H NMR spectrum (300 MHz) of [$LFe_3O(Pz)_3Mn(OH)$][OTf] (**6-[OTf]**; top) and [$LFe_3O(Pz)_3Mn(OH)$][BAr^F_4] (**6-[BAr^F_4]**; bottom) in CD_3CN.

---

^{1}H NMR and UV-Vis absorbance features, assigned to the Mn–OH cluster, **6-[BAr^F_4]**. Structural confirmation of this species was obtained by performing analogous reactions on **2-[OTf]** to prepare the triflate salt, **6-[OTf]**, which displays the same ^{1}H NMR features (Figure 8). This species could be crystallized from MeCN solution by slow diffusion of Et_2O, and was characterized via X-ray diffraction (Figure 4C). The structure of **6-[OTf]** is similar to **2-[OTf] (H_2O)**, displaying Mn binding to the hydroxide ligand with a trigonal bipyramidal geometry. Notably, the Mn–O distance to the hydroxide ligand is contracted by approximately 0.3 Å relative to **2-[OTf] (H_2O)** (1.843(9) vs 2.163(6) Å). Furthermore, the distance of the apical Mn to the interstitial μ_4-O in the cluster is also shortened significantly (1.838(8) vs 2.064(5) Å in **2-[OTf] (H_2O)**; Table 1); both of these observations are consistent with a Mn^{III}–OH assignment.[23] The Mn–OH and Mn–μ_4-O distances of ~1.8 Å are similar to the bond metrics observed in our previously reported hydroxide-bound tetramanganese cluster in the [$Mn^{III}_2Mn^{II}_2$] oxidation state.[19] There, the Mn–OH bond is slightly longer (1.872(2) Å) due to hydrogen bonding to the pendant *tert*-butyl-phenyl-aminopyrazolate ligands. The structural data for **6-[OTf]** are consistent to an oxidation state assignment of [$Fe^{II}_2Fe^{III}Mn^{III}$] for the

cluster; corroborated by the Mössbauer spectrum of **6-[BAr$^{F}_{4}$]** (Figure 9B). Deprotonation of the Mn^{II}–OH_2 in **2** to form **6** leads to rearrangement of the redox states of the metals in the cluster to produce a Mn^{III}–OH site. Similar 'valence tautomerizations' have been observed in Mn^{V}(O)-corrole systems, where protonation or binding a Lewis acid to the oxo moiety leads to reversible formation of a Mn^{IV}(O–X)-(corrole-radical cation) complexes.[24]

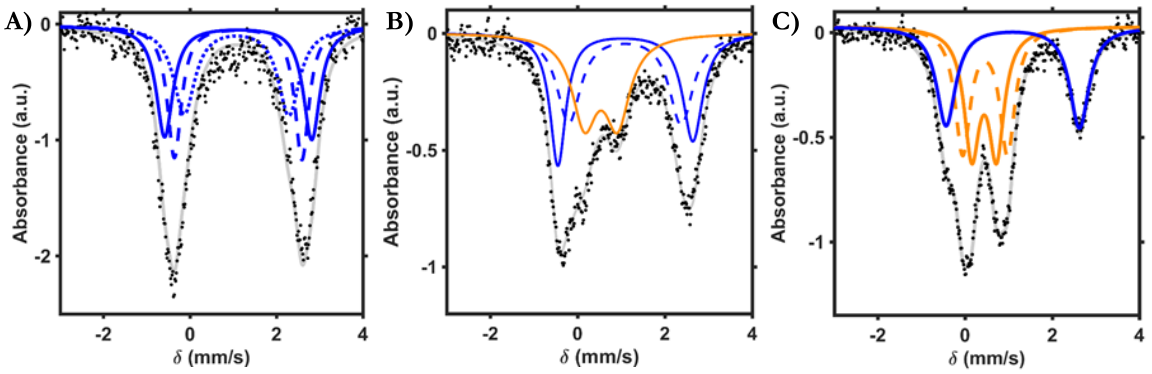

Figure 9. (A) Mössbauer spectrum of **5** (black dots) fit with three equal doublets (gray trace) with parameters: (i) δ = 1.12 mm/s; ΔE_q = 3.40 mm/s (solid blue trace), (ii) δ = 1.12 mm/s; ΔE_q = 2.95 mm/s (dashed blue trace), and (iii) δ = 1.08 mm/s; ΔE_q = 2.42 mm/s (dotted blue trace). (B) Mössbauer spectrum of **6-[BAr$^{F}_{4}$]** (THF solution [250 mM H_2O]; black dots) fit with three equal doublets (gray trace) with parameters: (i) δ = 1.09 mm/s; ΔE_q = 3.09 mm/s (solid blue trace), (ii) δ = 1.08 mm/s; ΔE_q = 2.58 mm/s (dashed blue trace), and (iii) δ = 0.53 mm/s; ΔE_q = 0.76 mm/s (solid orange trace). (C) Mössbauer spectrum of **7-[BAr$^{F}_{4}$]** (THF solution [250 mM H_2O]; black dots) fit with three equal doublets (gray trace) with parameters: (i) δ = 1.10 mm/s; ΔE_q = 3.03 mm/s (solid blue trace), and (ii) δ = 0.43 mm/s; ΔE_q = 0.55 mm/s (solid orange trace), (iii) δ = 0.46 mm/s; ΔE_q = 1.02 mm/s (dashed orange trace).

Electrochemistry. The electrochemistry of the [$Fe_3OMn–OH_2$] and [$Fe_3OMn–OH$] clusters was investigated by cyclic voltammetry of **2-[BAr^F_4]** and **6-[BAr^F_4]**. Two quasi-reversible redox events were observed in **2-[BAr^F_4]**: an oxidation at -0.02 V and a reduction at -0.90 V (all potentials vs Fc/Fc^+; Figure 10, red trace). These redox events were assigned to the $[Fe^{III}_2Fe^{II}Mn^{II}]\rightarrow[Fe^{III}_3Mn^{II}]$ and $[Fe^{III}Fe^{II}_2Mn^{II}]\rightarrow[Fe^{III}_2Fe^{II}Mn^{II}]$ couples. Mössbauer spectra collected on **1-[BAr^F_4]** – **3-[BAr^F_4]** in THF with 250 mM H_2O show that both oxidation state changes occur at the Fe centers (Figure 11), leading to the conclusion that the apical Mn remains divalent when bound to H_2O across all the oxidation states observed in the CV experiment, and only the distal Fe centers change oxidation states. The hydroxide-bound cluster, **6-[BAr^F_4]**, displays two oxidations: a quasi-reversible couple at -0.49 V ($[Fe^{III}Fe^{II}_2Mn^{III}]\rightarrow[Fe^{III}_2Fe^{II}Mn^{III}]$), and an irreversible event at +0.26 V ($[Fe^{III}_2Fe^{II}Mn^{III}]\rightarrow[Fe^{III}_3Mn^{III}]$). A quasi-reversible reduction for the $[Fe^{III}Fe^{II}_2Mn^{III}]\rightarrow[Fe^{II}_3Mn^{III}]$ couple is also observed at -1.34 V. The Mössbauer spectra of **5** - **7-[BAr^F_4]** (Figure 9) are again consistent with redox changes occurring exclusively at Fe. Notably, no catalytic oxidation wave is observed at high potentials for **6-[BAr^F_4]**, in contrast to our previously reported tetramanganese cluster bridged with *tert*-butyl-phenylaminopyrazolates.[19] Reasons for this difference may be the ~100 mV negative shift in reduction potentials for the [$Fe_3Mn–OH$] clusters, along with the lower concentration of H_2O. The lack of electrocatalytic oxidation by **6-[BAr^F_4]** could also suggest the importance of pendant basic groups near the Mn^{III}–OH moiety for water oxidation catalysis.

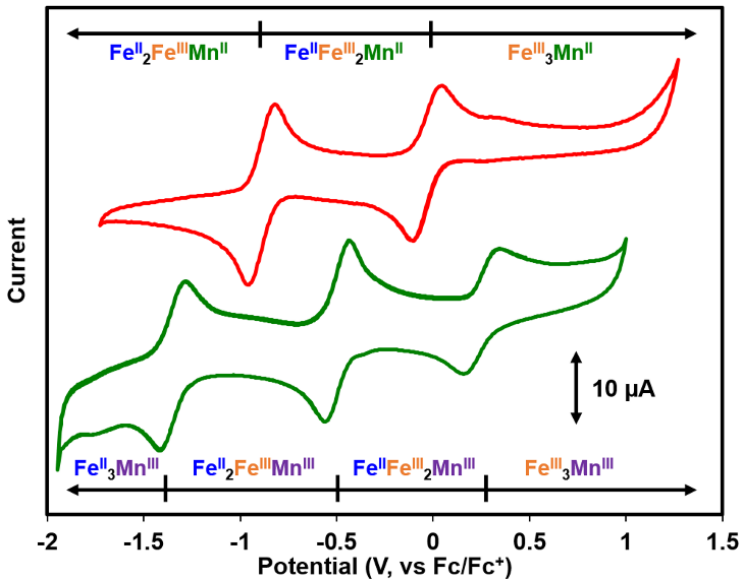

Figure 10. Cyclic voltammograms of **2-[BAr$^F_4$]** (red trace) and **6-[BAr$^F_4$]** (green trace); 2 mM compound in THF with 250 mM H_2O and 100 mM [^{n}Pr$_4$N][BAr$^F_4$] at a scan rate of 50 mV/s with glassy carbon, Pt-wire, and Ag-wire as working, counter, and reference electrodes, respectively. The open circuit potentials were -0.2 V for **2-[BAr$^F_4$]** and -1.0 V for **6-[BAr$^F_4$]**.

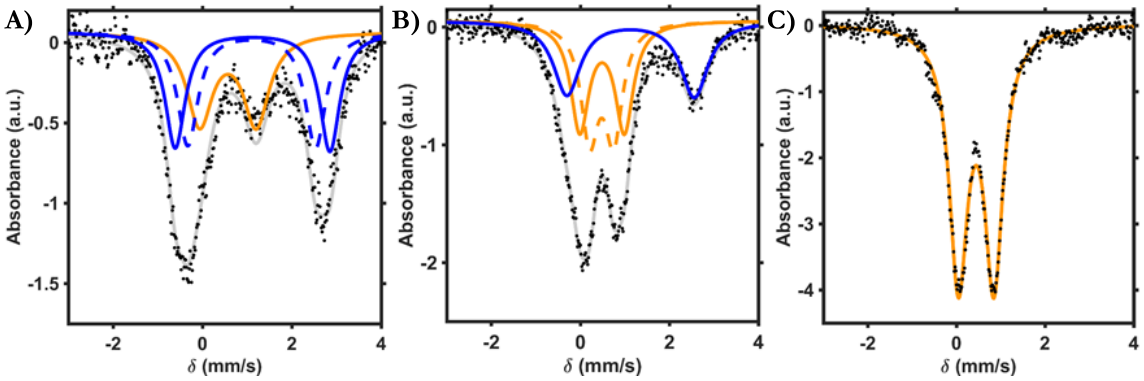

Figure 11. (A) Mössbauer spectrum of **1-[BAr$^F_4$]** (THF solution [250 mM H_2O]; black dots) fit with three equal doublets (gray trace) with parameters: (i) δ = 1.12 mm/s; ΔE_q = 3.46 mm/s (solid blue trace), (ii) δ = 1.10 mm/s; ΔE_q = 2.86 mm/s (dashed blue trace), and (iii) δ = 0.57 mm/s; ΔE_q = 1.27 mm/s (solid orange trace). (B) Mössbauer spectrum of **2-[BAr$^F_4$]** (THF solution [250 mM H_2O]; black dots) fit with three equal doublets (gray trace) with parameters:

(i) δ = 1.13 mm/s; ΔE_q = 2.86 mm/s (solid blue trace), (ii) δ = 0.49 mm/s; ΔE_q = 1.00 mm/s (solid orange trace), and (iii) δ = 0.48 mm/s; ΔE_q = 0.546 mm/s (dashed orange trace). (C) Mössbauer spectrum of **3-[BAr$^F_4$]** (THF solution [250 mM H_2O]; black dots) fit with a single quadrupole doublet (orange trace) with parameters: δ = 0.44 mm/s and ΔE_q = 0.80 mm/s

---

Determination of pK_a of H_2O Ligand in [Fe_3Mn^{II}–OH_2] Clusters. The pK_a of the aquo-ligand bound to 2-[BAr$^F_4$] was measured by mixing this cluster with various concentrations of 1,1,3,3-tetramethyl-2-phenylguanidine (PhTMG; pK_a(THF) = 16.5).[22] The ratio of **2-[BAr$^F_4$]** and **6-[BAr$^F_4$]** was examined by UV-Vis absorbance spectroscopy as a function of PhTMG concentration, and a pK_a value of 17.5 for **2-[BAr$^F_4$]** was obtained (Figure 12). Analogous experiments were attempted on the oxidized aquo-cluster, **3-[BAr$^F_4$]**; however, the changes in UV-Vis spectral features upon deprotonation are minor. The pK_a of **3-[BAr$^F_4$]** could be obtained by examining its ^{1}H NMR resonances in the presence of a suitable exogenous base, 2,6-Me_2-pyridine (Figure 13; pK_a(THF) = 9.5).[22] As expected, the acidity of the [Fe_3Mn–OH_2] cluster increases upon oxidation; a pK_a value of 9.2 was obtained for **3-[BAr$^F_4$].** While a titration on the reduced [$Fe^{III}Fe^{II}_2Mn^{II}$] cluster, **1-[BAr$^F_4$]**, was not conducted, we determined that its pK_a is significantly higher than the other clusters investigated, since it does not react with excess DBU (Figure 5; pK_a(THF) = 19.1).[22]

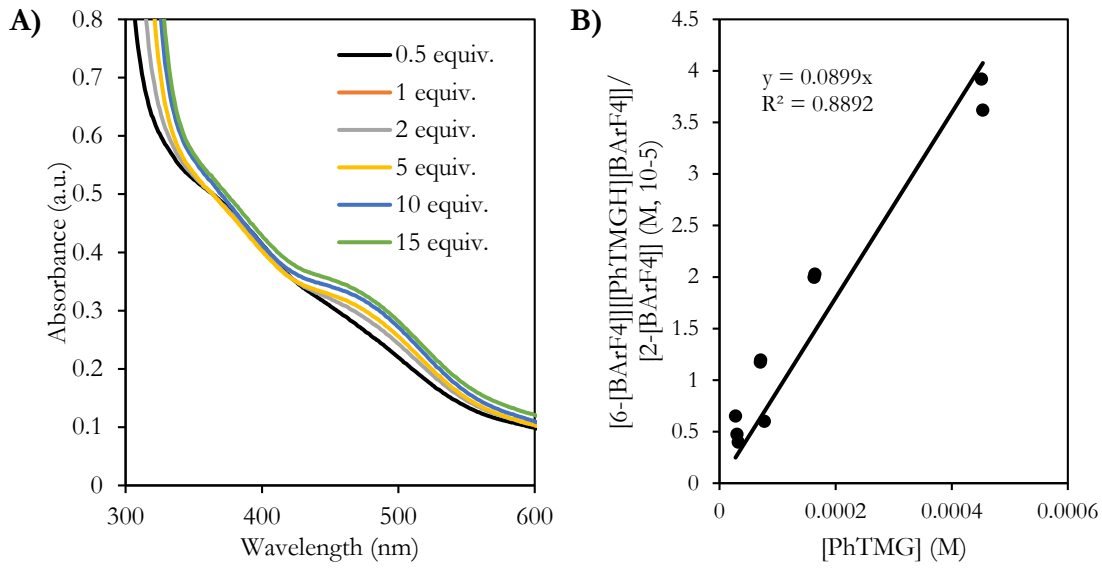

Figure 12. (A) UV-Vis absorbance spectra of $[LFe_3O(Pz)_3Mn][BAr^F{}_4]_2$ (**2-[BAr$^F{}_4$]**; 1 cm cuvette; 100μM) in THF [250 mM H_2O] after addition of various equivalents of 1,1,3,3-tetramethyl-2-phenylguanidine (PhTMG; pK_a(THF) = 16.5).[22] (B) Titration plot for deprotonation of $[LFe_3O(Pz)_3Mn][BAr^F{}_4]_2$ (**2-[BAr$^F{}_4$]**) to $[LFe_3O(Pz)_3Mn(OH)][BAr^F{}_4]$ (**6-[BAr$^F{}_4$]**) based on multiple titrations; the slope of the line represents an equilibrium constant value of $K = 0.09$, where:

$$K = \frac{[\mathbf{6}\text{–}[\mathbf{BAr^F_4}]][(\text{PhTMGH})([BAr^F_4])]}{[\mathbf{2}\text{–}[\mathbf{BAr^F_4}]][\text{PhTMG}]}$$

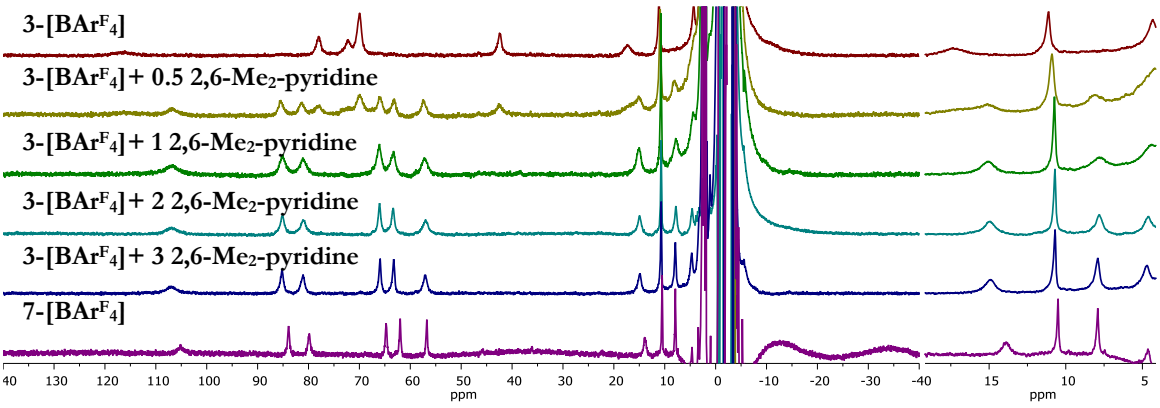

Figure 13. ^{1}H NMR spectrum (500 MHz) of $[LFe_3O(Pz)_3Mn][BAr^F{}_4]_3$ (**3-[BAr$^F{}_4$]**) with various equivalents of 2,6-dimethyl-pyridine in THF/C_6D_6 [250 mM H_2O].

Table 2. pK_a titration of 3-[BAr$^F{}_4$] via ^{1}H NMR spectroscopy with 2,6-dimethyl-pyridine.

^{1}H NMR	δ[a] (ppm)	$X_{\mathbf{3\text{-}[BArF4]}}$[b]	K[c]
3-[BAr$^F{}_4$]	11.12	-	
3-[BAr$^F{}_4$] + 0.5 2,6-Me$_2$-Py	10.90	0.632	1.625
3-[BAr$^F{}_4$] + 1 2,6-Me$_2$-Py	10.72	0.343	3.661
3-[BAr$^F{}_4$] + 2 2,6-Me$_2$-Py	10.70	0.319	1.100
3-[BAr$^F{}_4$] + 3 2,6-Me$_2$-Py	10.69	0.296	0.730
7-[BAr$^F{}_4$]	10.51	-	
		Average K	1.779 (±0.654)

[a]A sharp resonance ~ 11 ppm was selected to measure the mole fraction of **3-[BAr$^F{}_4$]** ($X_{\mathbf{3\text{-}[BArF4]}}$), as **3-[BAr$^F{}_4$]** and **7-[BAr$^F{}_4$]** undergo fast exchange on the NMR time-scale. [b] The concentrations of **3-[BAr$^F{}_4$]**, 2,6-Me$_2$-Py, and [2,6-Me$_2$-PyH][BAr$^F{}_4$] were determined from $X_{\mathbf{3\text{-}[BArF4]}}$ via mass balance. [c]According to the equation below:

$$K = \frac{[\mathbf{7}\text{–}[\mathbf{BAr}_4^F]][(2,6\text{–}\mathrm{Me_2}\text{–}\mathrm{PyH})([\mathrm{BAr}_4^F])]}{[\mathbf{3}\text{–}[\mathbf{BAr}_4^F]][2,6\text{–}\mathrm{Me_2}\text{–}\mathrm{Py}]}$$

BDE$_{O–H}$ and PCET Reactivity of the Different Redox States. The homolytic bond dissociation enthalpy of the aquo O–H (BDE$_{O–H}$) were determined for the three cluster oxidation states observed (**1-[BAr$^F{}_4$]** – **3**-**[BAr$^F{}_4$]**) by analyzing the pK_a and reduction potentials of the aquo- and hydroxide-bound clusters (Figure 14). This calculation combines the energies of the discrete proton and electron transfers involved, along with the energy of formation of the hydrogen atom in THF (C; 66 kcal/mol[25]):[26]

$$\mathrm{BDE_{O–H}}\ (\mathrm{kcal/mol}) = 1.37\ \mathrm{p}K_a + 23.06\ E° + C \qquad (1)$$

Therefore, summing the energy of the oxidation of **1-[BAr$^F{}_4$]** (-0.90 V; -20.6 kcal/mol) and the energy of deprotonation of **2-[BAr$^F{}_4$]** (17.5; 24.0 kcal/mol) with C establishes an energy of 69 kcal/mol for the formal H-atom transfer from **1-[BAr$^F{}_4$]** to **6-[BAr$^F{}_4$]**. Likewise, the oxidation of **2-[BAr$^F{}_4$]** (-0.02 V; -0.5 kcal/mol) followed by the deprotonation of **3-[BAr$^F{}_4$]** (9.2; 12.6 kcal/mol) leads to a BDE$_{O–H}$ of 78 kcal/mol for the aquo-ligand of **2-[BAr$^F{}_4$]** (formal HAT to form **7-[BAr$^F{}_4$]**). An alternate way to determine the BDE$_{O–H}$ of **2-[BAr$^F{}_4$]** is from the pK_a of **2-[BAr$^F{}_4$]** and the reduction potential of **6-[BAr$^F{}_4$]**, leading to a similar bond enthalpy of 78.7 kcal/mol. The same square scheme analysis can be done to obtain a BDE$_{O-H}$

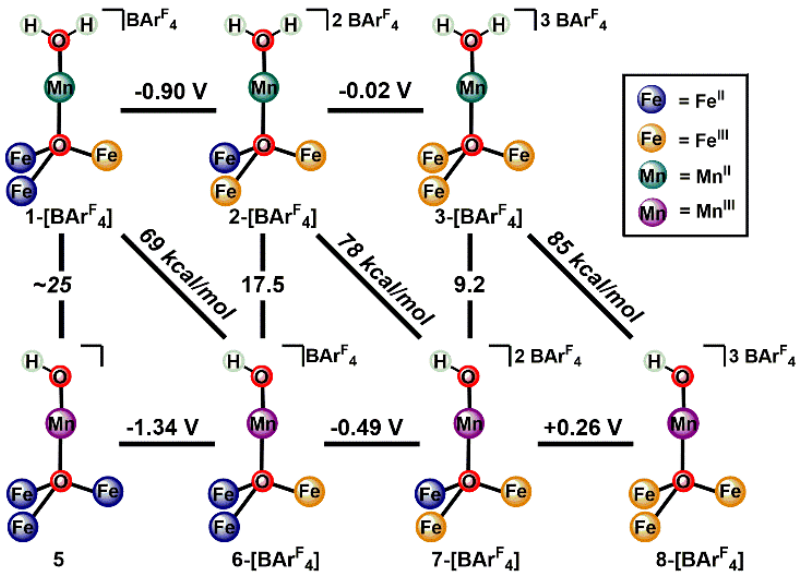

Figure 14. Thermodynamic cycles to evaluate the BDE_{O-H} of Mn–OH_2 clusters **1-[BAr^F_4]** - **3-[BAr^F_4]**. Reduction potentials (horizontal lines) are referenced to Fc/Fc^+. pK_a values (vertical lines) are based on relative pK_a values of acids in THF. Diagonal lines are the BDE_{O-H} values calculated from the reduction potential and pK_a according to the Bordwell equation (equation 1). Approximate values (~) are extrapolated from the Bordwell equation.

---

of 85 kcal/mol for **3-[BAr^F_4]**. With these measured values, the pK_a of **1-[BAr^F_4]** could be estimated; a BDE_{O-H} of 69 kcal/mol for **1-[BAr^F_4]** means the enthalpy of deprotonation for this cluster is expected to be ~34 kcal/mol (pK_a = 24.9), by combining this energy with the oxidation of **5** (-1.34 V; -30.9 kcal/mol).

The BDE_{O-H} values of these clusters were evaluated by investigating their proton-coupled electron transfer (PCET) reactivity towards different organic radicals. The PCET reagents employed were (2,2,6,6,-tetramethylpiperidin-1yl)oxyl (TEMPO; BDE_{O-H} = 70 kcal/mol) and 2,4,6-tri-*tert*-butylphenoxy radical (2,4,6-TBPR; BDE_{O-H} = 82 kcal/mol).[26c] Formal hydrogen atom transfer from **1-[BAr^F_4]** to form **6-[BAr^F_4]** could be accomplished using either one equivalent of TEMPO or 2,4,6-TBPR, consistent with a BDE_{O-H} less than 70 kcal/mol

(Scheme 2). **2-[BAr$^F_4$]** reacts with 1 equivalent 2,4,6-TBPR to form **7-[BAr$^F_4$]**, but no reaction is observed between this cluster and TEMPO, indicative of a BDE_{O-H} that is between 70 and 82 kcal/mol. **3-[BAr$^F_4$]** does not react with either PCET reagent, which supports the assignment of a BDE_{O-H} greater than 82 kcal/mol).

Scheme 2. Proton Coupled Electron Transfer (PCET) Reactions of Mn–OH_2 clusters, 1-[BAr$^F_4$] - 3-[BAr$^F_4$].

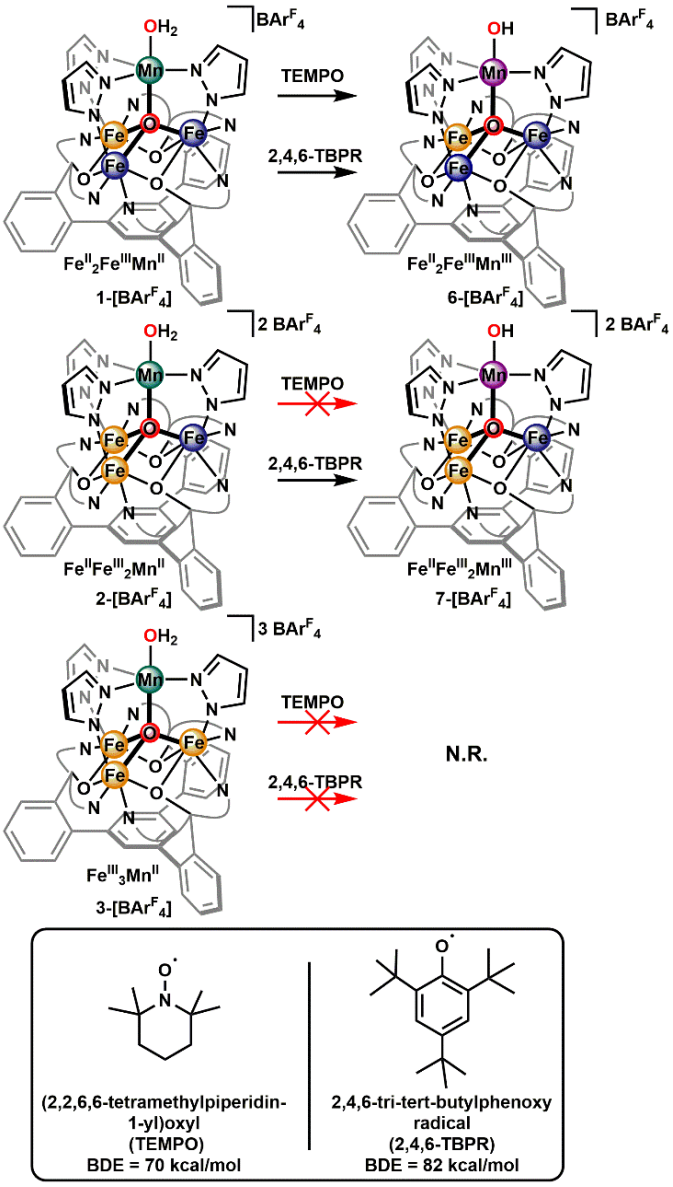

Potential–pK_a Diagram of [$Fe_3Mn–OH_x$] Clusters. Further insight into the basis of PCET reactivity of these clusters was obtained by investigating the effect of external bases on the reduction potentials of the aquo- and hydroxide-bound clusters. Typically, this type of analysis is conducted under aqueous conditions, where the reduction potentials can be measured as a function of solution pH; data are presented as a potential–pH plot, known as a Pourbaix diagram.[27] Aqueous Pourbaix diagrams have been helpful in understanding the speciation of a number of molecular Ru/Mn water oxidation catalysts and related complexes.[15b, 28] Recently, Pourbaix theory has been applied to nonaqueous solvents, where the reduction potential of PCET will depend on the pK_a of an external acid/base (and the concentration of this acid/base relative to its conjugate base/acid at Nernstian equilibrium).[29] For the system reported here, a potential– pK_a plot was constructed as a means of providing experimental support for the aquo-ligand pK_a and $BDE_{O–H}$ values of **1-[BAr^F_4]** - **3-[BAr^F_4]** and to gain information about the thermochemistry of PCET with the Mn–OH clusters to form a terminal Mn-oxo moiety.

Measuring the CV of **2-[BAr^F_4]** with one equivalent of various organic bases, with pK_a values of their conjugate acids in THF ranging from 7.5 to 28.1, produced the potential–pK_a plot depicted in Figure 15 (blue points; see Electrochemical Details section for individual CVs). For relatively weak bases (pK_a < 10), the reduction potentials of **2-[BAr^F_4]** do not significantly deviate from their potentials in the absence of any base. As the strength of the base increases, the reduction potential for the oxidation of **2-[BAr^F_4]** is lowered as a function of the conjugate acid pK_a, consistent with PCET occurring between the pK_a range 10-17. The data points in this pK_a range follow the diagonal line calculated for the **2-[BAr^F_4]→7-[BAr^F_4]** PCET process, based on the reduction potentials of **2-[BAr^F_4]** and **6-[BAr^F_4]** and the pK_a values of **2-[BAr^F_4]** and **3-[BAr^F_4]**. Observing the predicted linear decrease in reduction

potential for **3-[BAr$^{F}_{4}$]** in the pK_a range 10 - 17 supports the pK_a values reported for **2-[BAr$^{F}_{4}$]** and **3-[BAr$^{F}_{4}$]** in Figure 14. Similar support is given to the pK_a of **1-[BAr$^{F}_{4}$]** (24.9) when using strong bases (pK_a > 17.5). Evidence for the **1-[BAr$^{F}_{4}$]→6-[BAr$^{F}_{4}$]** PCET process was observed under these conditions, again with the data roughly matching the diagonal line with an intercept at -1.34 V and a pK_a of 24.9. Furthermore, when a base was employed with a pK_a > 24.9, the reduction potentials observed were nearly identical to the potentials reported for **6-[BAr$^{F}_{4}$]** in the absence of any acid or base.

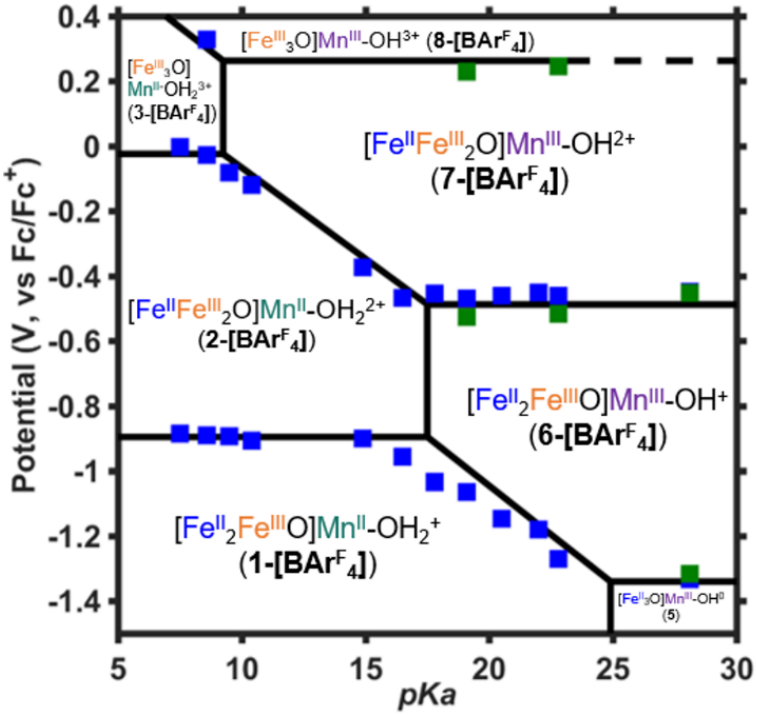

Figure 15. Potential–pK_a diagram of **2-[BAr$^{F}_{4}$]** (blue squares) and **6-[BAr$^{F}_{4}$]** (green squares). Data points are the observed reduction potentials of the compounds (y-axis) in the presence of one equivalent base with various pK_a values in THF (x-axis). The horizontal lines correspond to the measured reduction potentials of **2-[BAr$^{F}_{4}$]** and **6-[BAr$^{F}_{4}$]** in the absence of any external base. Vertical lines correspond to the pK_a values of Mn–OH$_2$ clusters **1-[BAr$^{F}_{4}$]** - **3-[BAr$^{F}_{4}$]**. The horizontal line for the **7-[BAr$^{F}_{4}$]→8-[BAr$^{F}_{4}$]** redox couple is dashed at high pK_a values due to the possibility of PCET from the Mn–OH with a strong enough base.

As expected, deviations of the data from the calculated diagonal line occur as the base pK_a approaches the pK_a of the cluster (see **2-[BAr$^F_4$]→7-[BAr$^F_4$]** around pK_a of 10, for example), based on predicted potential–pK_a relationships for ET-PT or PT-ET reaction mechanisms.[29] Further deviations from the predicted solid lines in Figure 15 could be due to incompatibility of the chosen base with this system (too coordinating, electrochemically unstable, etc.). Ultimately, inconsistencies between the potential–pK_a data of **2-[BAr$^F_4$]** and the BDE$_{O–H}$ values reported in Figure 14 only amount to a difference of ~3 kcal/mol, which is a reasonable uncertainty for these bond energydeterminations.[26c] Based on the PCET reactivity of these complexes towards TEMPO and TBPR (vide supra), it is unlikely that these BDE$_{O–H}$ values could deviate more than a few kcal/mol.

Potential–pK_a data were also obtained for **6-[BAr$^F_4$]** in the presence of relatively strong organic bases in attempts to observe a PCET process accessing Mn=O clusters, since this technique has been previously useful for gaining insight into the proton and electron transfer thermodynamics for unstable species.[29] Based on the potential–pK_a plot constructed in Figure 15, PCET to form a Mn-oxo cluster could be possible at high potentials with a strong base (top right area of the diagram). The CV of **6-[BAr$^F_4$]** with one equivalent *tert*-butylimino-tri(pyrrolidino)phosphorene (*t*-BuP$_1$(pyrr); pK_a(THF) = 22.8)[22] shows no shift in the Mn–OH cluster reduction potentials. Similarly, no change is observed with the **5→6-[BAr$^F_4$]** and **6-[BAr$^F_4$]→7-[BAr$^F_4$]** reduction potentials with 1-ethyl-2,2,4,4,4-pentakis(dimethylamino)2-λ^5,4λ^5-catenadi(phosphazene) (EtP$_2$(dma); pK_a(THF) = 28.1).[22, 30] These experimental observations provide a lower limit to the pK_a values of **8-[BAr$^F_4$]** and **7-[BAr$^F_4$]**, respectively. With these values, the BDE$_{O–H}$ of **7-[BAr$^F_4$]** and **8-[BAr$^F_4$]** are predicted to be greater than 93 and 103 kcal/mol, respectively (Figure 16).[31] These BDE$_{O–H}$ estimates are higher than Mn complexes, where these bond strengths have been reported.[11c, 12d, 12i, 12k] The large BDE$_{O–H}$

values for these hydroxide clusters suggest that if these terminal oxo moieties could be accessed, they would be highly reactive. Indeed, previous attempts to generate a terminal oxo species on related phenyl-pyrazolate bridged multimetallic clusters results in activation of strong bonds, although the identity of the reactive intermediate in these reactions could not be established (terminal metal-oxo or iodosylbenzene adduct).[18d-f]

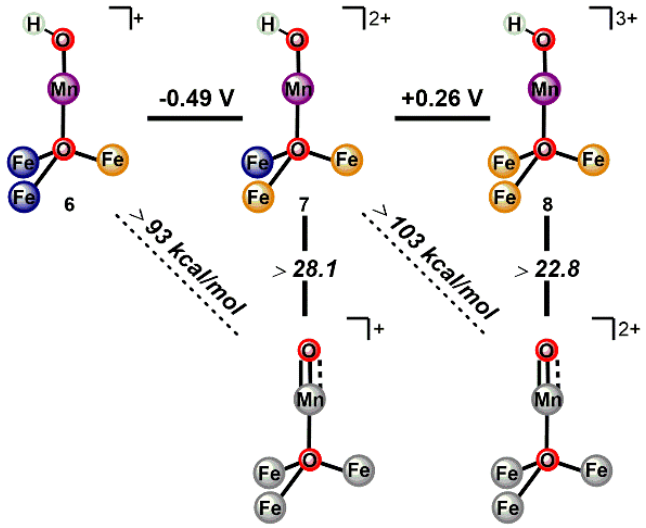

Figure 16. Estimated BDE_{O-H} values for Mn^{III}–OH clusters **6-[BAr$^F_4$]** and **7-[BAr$^F_4$]** based on their oxidation potentials and lower bound of their pK_a (where no PCET occurs in their CV with an external base). The metal oxidation states of the resulting putative Mn-oxo clusters are left ambiguous since multiple oxidation state distributions are possible.

CONCLUSIONS

We have reported the synthesis of tetranuclear [Fe_3Mn–OH_x] clusters bearing bridging unsubstituted pyrazolate ligands, leading to a sterically open coordination environment around the apical Mn center. These clusters were used to investigate the implications of distal metal redox changes on the activation of water by Mn in terms of the aquo-cluster pK_a, reduction potential, and homolytic O–H bond strength. Increasing the oxidation state of a distal Fe

center by one increases the acidity of the aquo ligand by ~7 pKa units (in THF), while raising the $BDE_{O–H}$ 8 kcal/mol, on average. By only changing the redox states of the distal Fe centers, a wide range of $BDE_{O–H}$ values could be measured for the Mn–OH_2 moiety (69 – 85 kcal/mol), which nearly spans the range of the reported $BDE_{O–H}$ measured in reported in mononuclear Mn–OH_2 complexes.[11c, 12e, 12f, 12i] The three different oxidation states of the aquo-cluster (**1-[BAr^F_4]** – **3-[BAr^F_4]**) underwent PCET reactions with TEMPO and 2,4,6-TBPR consistent with their measured $BDE_{O–H}$ values. The increase in $BDE_{O–H}$ of ~8 kcal/mol by increasing distal Fe oxidation state is similar to the increases that have been observed in mononuclear Mn systems where $BDE_{O–H}$ studies could be accomplished over multiple Mn oxidation states.[12d, 12i] This is in contrast to the previous example of a binuclear Mn system, where Mn–OH_2 $BDE_{O–H}$ values could be measured over three oxidation states, where small changes in the bond strength of ~ 4 kcal/mol for the $Mn^{III}Mn^{IV}$–OH_2 complex versus $Mn^{III}{}_2$–OH_2 were observed.[15a]

Importantly, the large effect of the remote metals on the $BDE_{O–H}$ demonstrates that the cluster as a whole has a significant impact in the activation of substrate water molecules. The range of $BDE_{O–H}$ reported here is achieved without change in the redox state of Mn; therefore, consideration of the effect of metal centers not directly supporting the substrate must be taken into account for multimetallic biological active sites as well as synthetic clusters. Additionally, the present findings demonstrate that, in comparison to monometallic complexes, transition metal clusters not only provide the possibility of increased storage of redox equivalents, but also can serve to dynamically tune reactivity through remote oxidation state changes.

EXPERIMENTAL DETAILS

General Considerations. All reactions were performed at room temperature in an N_2-filled M. Braun glovebox or using standard Schlenk techniques unless otherwise specified; reactions of compounds in THF/H_2O mixtures were performed in an N_2-filled VAC wetbox. Glassware was oven dried at 140 ºC for at least 2 h prior to use, and allowed to cool under vacuum. **[LFe$_3$(OAc)(OTf)][OTf]**[18a], Mn(OTf)$_2$ • 2 MeCN[32], benzyl potassium[33], iodosobenzene[34], silver tetrakis[3,5-bis(trifluoromethyl)phenyl]borate bis-acetonitrile (Ag[BAr$^F_4$] • 2 MeCN)[35], 2,4,6-tri-tert-butylphenoxy radical (2,4,6-TBPR)[36], and tetrapropylammnoium tetrakis[3,5-bis(trifluoromethyl)phenyl]borate ([^{n}Pr$_4$N][BAr$^F_4$])[37] were prepared according to literature procedures. All organic solvents were dried by sparging with nitrogen for at least 15 minutes, then passing through a column of activated A2 alumina under positive N_2 pressure. ^{1}H and ^{19}F NMR spectra were recorded on a Varian 300 MHz spectrometer. ^{1}H NMR spectra in THF/C_6D_6 were recorded on a Varian 500 MHz spectrometer using solvent suppression protocols. CD_3CN, CD_2Cl_2, and C_6D_6 were purchased from Cambridge Isotope Laboratories, dried over calcium hydride, degassed by three freeze-pump-thaw cycles, and vacuum transferred prior to use.

Physical Methods. *Mössbauer measurements*. Zero field ^{57}Fe Mossbauer spectra were recorded at 80 K in constant acceleration mode on a spectrometer from See Co (Edina, MN) equipped with an SVT-400 cryostat (Janis, Wilmington, WA). The isomer shifts are relative to the centroid of an α-Fe foil signal at room temperature. Samples were prepared by mixing polycrystalline material (20 mg) with boron nitride in a cup fitted with screw cap or freezing a concentrated solution in MeCN or THF. The data were fit to Lorentzian lineshapes using WMOSS (www.wmoss.org).

Mössbauer simulation details for all compounds. All spectra were simulated by three pairs of symmetric quadrupole doublets with equal populations and Lorentzian lineshapes. They were refined to a minimum via least squares optimization (13 fitting parameters per spectrum). Signals appearing above 2 mm/s were indicative with the presence of high-spin Fe^{II} centers and correspond to species with isomer shifts of ~ 1 mm/s. The Mössbauer data were fit to be consistent with our previously reported iron clusters.[17a, 18a, 18d, 18e] The observed Mossbauer parameters are in agreement with related six-coordinate high-spin Fe^{II}/Fe^{III} centers.[38]

Electrochemical measurements. CVs and SWVs were recorded with a Pine Instrument Company AFCBP1 biopotentiostat with the AfterMath software package. All measurements were performed in a three electrode cell, which consisted of glassy carbon (working; ø = 3.0 mm), silver wire (counter) and bare platinum wire (reference), in a N_2 filled M. Braun glovebox at RT. Either the ferrocene/ferrocinium (Fc/Fc^+) or decamethylferrocene/ decamethylferrocinium (Fc^*/Fc^{*+}; -0.524 V vs Fc/Fc^+ in THF/250 mM H_2O, under our experimental conditions) redox waves were used as an internal standard for all measurements.

X-ray crystallography. X-ray diffraction data was collected at 100 K on a Bruker PHOTON100 CMOS based diffractometer (microfocus sealed X-ray tube, Mo Kα (λ) = 0.71073 Å or Cu Kα (λ) = 1.54178 Å). All manipulations, including data collection, integration, and scaling, were carried out using the Bruker APEXII software. Absorption corrections were applied using SADABS. Structures were solved by direct methods using XS (incorporated into SHELXTL) and refined by using ShelXL least squares on Olex2-1.2.7 to convergence. All non-hydrogen atoms were refined using anisotropic displacement parameters. Hydrogen atoms were placed in idealized positions and refined using a riding model. Due to the size of the compounds most crystals included solvent-accessible voids that contained disordered solvent. In most cases the solvent could be modeled satisfactorily.

Synthetic Procedures. *Synthesis of Potassium pyrazolate (KPz).* 1.09 g (16.0 mmol) pyrazole was dissolved in 2 mL THF. To this stirring solution, a 10 mL THF solution of benzyl potassium, 2.03 g (15.6 mmol), was added dropwise; an off-white precipitate formed. After stirring for 20 minutes, the reaction was concentrated to 10 mL; the solids were collected on a glass frit and washed with 2 mL THF. The white solid was dried completely under vacuum to obtain 1.37 g (83% yield) potassium pyrazolate. Anal. calcd. (%) for $C_3H_3KN_2$: C. 33.94; H, 2.85; N, 26.39. Found: C, 34.12; H, 2.89; N, 25.38.

*Synthesis of [LFe₃O(Pz)₃Mn][OTf]₂ (**2-[OTf]**).* A suspension of 387 mg (0.28 mmol) **[LFe₃(OAc)(OTf)][OTf]** in 7 mL THF was stirred with 98.4 mg (0.29 mmol) $Ca(OTf)_2$ for an hour before being frozen with LN_2. To this mixture, 93.2 mg (0.88 mmol) KPz was added in thawing THF (4 mL) and stirred for 20 minutes at room temperature to obtain a dark red-orange solution. Iodosylbenzene, 63.6 mg (0.29 mmol), was added with 1 mL THF and the reaction was stirred for 90 minutes. 160 mg (0.37 mmol) $Mn(OTf)_2 \bullet 2$ MeCN solution in 2 mL THF was then added to the reaction. After 18 hours, the reaction was concentrated to 10 mL and filtered over a bed of celite; the precipitate was dried under vacuum, extracted with 8 mL DCM, and recrystallized via vapor diffusion of Et_2O into the filtrate. Dark green crystals of **2-[OTf]** were collected on a glass frit and dried (147 mg, 33% yield). Another 69 mg of **2-[OTf]** can be obtained by drying the crude reaction filtrate, extracting with 6 mL DCM and recrystallizing via Et_2O vapor diffusion (46% overall yield). X-ray diffraction quality crystals were obtained via oxidation of $[LFe_3O(Pz)_3Mn][OTf]$ (**1-[OTf]**) with 1 equivalent of $AgBPh_4$; Et_2O vapor diffusion into a DCM/THF solution of the resulting $[LFe_3O(Pz)_3Mn][OTf][BPh_4]$ produced crystals of suitable quality. ^1H NMR (300 MHz, CD_3CN): δ 120.8 (br), 80.8 (br), 71.0, 70.1, 52.9, 52.3, 42.2, 28.0 (br), 15.5, 13.0, 10.4, 8.1 (br), 4.38, 3.01, -2.51 (br). UV-Vis

(MeCN) [ε (M^{-1} cm^{-1})] 241 nm (6.53× 10^4), 368 nm (6.49 × 10^3). Anal. calcd. (%) for $C_{68}H_{48}F_6Fe_3MnN_{12}O_{10}S_2$: C. 51.25; H, 3.04; N, 10.55. Found: C, 50.81; H, 3.12; N, 10.18.

*Synthesis of [LFe₃O(Pz)₃Mn][OTf] (**1-[OTf]**).* A suspension of $[LFe_3O(Pz)_3Mn][OTf]_2$ (**2-[OTf]**; 91.5 mg, 0.057 mmol) in 2 mL THF was stirred as a THF solution of 10.9 mg $CoCp_2$ (0.058 mmol) was added. After 1 hour, the reaction was dried under vacuum. 4 mL DME was added to the purple solid and stirred for 12 hours. The resulting purple precipitate was collected on a bed of celite, washed with 2 mL DME, dried, and eluted with 2:1 THF/MeCN; crystals of $[LFe_3O(Pz)_3Mn][OTf]$ (**1-[OTf]**) were obtained by vapor diffusion of Et_2O into this solution (46.3 mg, 56% yield). ^{1}H NMR (300 MHz, CD_3CN): δ 96.4 (br), 57.8, 55.5, 37.8 (br), 36.4, 34.3, 34.0, 25.2, 13.4, 13.0, 12.0, 11.4, 3.4, 2.6, -6.4 (br). UV-Vis (MeCN) [ε (M^{-1} cm^{-1})] 250 nm (6.08 × 10^4), 517 nm (3.72 × 10^3). Anal. calcd. (%) for $C_{67}H_{48}F_3Fe_3MnN_{12}O_7S$: C, 55.70; H, 3.35; N, 11.63. Found: C, 55.36; H, 3.58; N, 11.20.

*Synthesis of [LFe₃O(Pz)₃Mn][OTf]₃ (**3-[OTf]**).* 9.2 mg (0.036 mmol) of AgOTf in THF was added to a stirring suspension of 56.8 mg (0.036 mmol) $[LFe_3O(Pz)_3Mn][OTf]_2$ (**2-[OTf]**) in THF. The resulting brown suspension was pumped down after 30 minutes. The reaction was filtered over a celite pad using DCM and the solvent was removed under reduced pressure. Crystals of $[LFe_3O(Pz)_3Mn][OTf]_3$ were obtained via vapor diffusion of Et_2O into a concentrated DCM/MeCN solution of the crude product, 57.4 mg (92% yield). ^{1}H NMR (300 MHz, CD_2Cl_2): δ 162.2 (br), 118.9 (br), 81.2, 76.9, 74.4, 73.1, 45.7, 18.8 (br), 16.3, 9.5, 3.34, 1., -6.5 (br). UV-Vis (MeCN) [ε (M^{-1} cm^{-1})] 241 nm (7.84 × 10^4), 411 nm (9.22 × 10^3). Anal. calcd. (%) for $C_{69}H_{48}F_9Fe_3MnN_{12}O_{13}S_3$: C, 47.55; H, 2.78; N, 9.64. Found: C, 47.57; H, 3.07; N, 9.21.

*Synthesis of [LFe₃O(Pz)₃Mn] (**4**).* 4.1 mg (0.18 mmol) sodium metal was mixed ~6 g elemental mercury with a pre-reduced stirbar. After 12 hours, a 5 mL THF suspension of $[LFe_3O(Pz)_3Mn][OTf]_2$ (**2-[OTf]**; 114 mg, 0.07 mmol) was added to the Na/Hg amalgam.

Over 4 hours, a blue precipitate formed; this resulting suspension was decanted from the amalgam and filtered over a fine porosity glass frit. The solids were washed with 5 mL THF and dried under vacuum. The resulting blue material, $[LFe_3O(Pz)_3Mn]$ (78.1 mg; 84% yield), is insoluble or unstable in most typical organic solvents. Anal. calcd. (%) for $C_{66}H_{48}Fe_3MnN_{12}O_4$: C. 61.18; H, 3.73; N, 12.94. Found: C, 60.44; H, 3.82; N, 12.87

Synthesis of $[LFe_3O(Pz)_3Mn][BAr^F{}_4]$ (***1-[BAr$^F{}_4$]***). 14.0 mg (0.013 mmol) $Ag[BAr^F{}_4]$ • 2 MeCN in 2 mL Et_2O was added to a stirring suspension of $[LFe_3O(Pz)_3Mn]$ (**4**; 17.2 mg, 0.013 mmol); the blue suspension changed to a purple solution. After 15 minutes, the solvent was removed under reduced pressure. 3 mL Et_2O was added to the purple residue and filtered over a pad of celite. The filtrate was dried to afford $[LFe_3O(Pz)_3Mn][BAr^F{}_4]$ as a purple solid, 26.5 mg (92% yield). ^{1}H NMR (300 MHz, CD_3CN) is identical to $[LFe_3O(Pz)_3Mn][OTf]$ (**1-[OTf]**). Anal. calcd. (%) for $C_{98}H_{60}BF_{24}Fe_3MnN_{12}O_4$: C. 54.52; H, 2.80; N, 7.79. Found: C, 54.06; H, 2.84; N, 7.33.

Synthesis of $[LFe_3O(Pz)_3Mn][BAr^F{}_4]_2$ (***2-[BAr$^F{}_4$]***). 45.0 mg (0.043 mmol) $Ag[BAr^F{}_4]$ • 2 MeCN in 2 mL Et_2O was added to a stirring suspension of $[LFe_3O(Pz)_3Mn]$ (**4**; 27.6 mg, 0.021 mmol); the blue suspension changed to a brown-green solution. After 15 minutes, the solvent was removed under reduced pressure. 3 mL Et_2O was added to the brown residue and filtered over a pad of celite. 6 mL benzene was added to the filtrate to produce an oily precipitate; after 30 minutes, the supernatant was removed and the remaining brown-green residue was dried under reduced pressure. 36.6 mg (57% yield) of the brown-green solid, **2-[BAr$^F{}_4$]**, was obtained; the ^{1}H NMR (300 MHz, CD_3CN) is identical to $[LFe_3O(Pz)_3Mn][OTf]_2$ (**2-[OTf]**). UV-Vis (THF/250 mM H_2O) [ε (M^{-1} cm^{-1})] 368 nm (5.11×10^3). Anal. calcd. (%) for $C_{130}H_{72}B_2F_{48}Fe_3MnN_{12}O_4$: C. 51.67; H, 2.40; N, 5.56. Found: C, 51.38; H, 2.56; N, 5.46.

*Synthesis of [LFe$_3$O(Pz)$_3$Mn][BAr$^F{}_4$]$_3$ (**3-[BAr$^F{}_4$]**).* 6.4 mg (0.006 mmol) [^{Ac}Fc][BAr$^F{}_4$] in 0.5 mL THF was added to [LFe$_3$O(Pz)$_3$Mn][BAr$^F{}_4$]$_2$ (**2-[BAr$^F{}_4$]**; 18.6 mg, 0.006 mmol). After 10 minutes, 5 mL benzene was added to the solution to produce an oily brown precipitate; after 30 minutes, the yellow supernatant was removed and the remaining brown residue was dried under reduced pressure. 18.4 mg of a brown solid was obtained (77% yield). ^{1}H NMR (500 MHz, THF/C$_6$D$_6$ [250mM H$_2$O]): δ 83.8, 78.2, 75.9, 50.2, 24.9 (br), 16.6, 9.8 (br), 0.1. UV-Vis (THF/250 mM H$_2$O) [ε (M^{-1} cm^{-1})] 405 nm (7.64× 10^3). Anal. calcd. (%) for C$_{162}$H$_{84}$B$_3$F$_{72}$Fe$_3$MnN$_{12}$O$_4$: C. 50.08; H, 2.18; N, 4.33. Found: C, 50.34; H, 2.38; N, 4.29.

*Synthesis of [LFe$_3$O(Pz)$_3$Mn(OH)][BAr$^F{}_4$] (**6-[BAr$^F{}_4$]**).* Addition of 100 μL of a 50 mM solution of DBU in THF/250 mM H$_2$O to 2 mL 2 mM solution of [LFe$_3$O(Pz)$_3$Mn][BAr$^F{}_4$]$_2$ (**2-[BAr$^F{}_4$]**) in THF/250 mM H$_2$O leads to a color change of the solution from green to red. Crystals for X-ray diffraction (**6-[OTf]**) were obtained by conducting the analogous reaction with [LFe$_3$O(Pz)$_3$Mn][OTf]$_2$ (**2-[OTf]**) and DBU in 95:5 MeCN/H$_2$O and crystalizing via vapor diffusion of Et$_2$O into this solution; considerable decomposition occurs on the timescale of crystallization, making crystallization unsuitable for preparing analytically pure solid samples of [LFe$_3$O(Pz)$_3$Mn(OH)][OTf]. Solutions of [LFe$_3$O(Pz)$_3$Mn(OH)][BAr$^F{}_4$] were prepared for electrochemistry experiments by stirring 4 mL of 2.5 mM [LFe$_3$O(Pz)$_3$Mn][[BArF4]]$_2$ (**2-[BAr$^F{}_4$]**) and 0.1 M [^{n}Pr$_4$N][BAr$^F{}_4$] solution in THF/250 mM H$_2$O with ~2 mg of solid KOH pellet for 1 hour; the resulting red solution was decanted off the remaining KOH before electrochemical measurements were conducted. ^{1}H NMR (500 MHz, THF/C$_6$D$_6$ [250mM H$_2$O]): δ 153.1 (br), 102.7 (br), 85.9, 80.0, 64.8, 60.8, 58.1, 57.3, 23.0, 15.7. 12.5, 10.9 (br). UV-Vis (THF/250 mM H$_2$O) [ε (M^{-1} cm^{-1})] 467 nm (3.29 × 10^3).

*Synthesis of [LFe$_3$O(Pz)$_3$Mn(OH)] (**5**).* Addition of 11 mg (0.03 mmol) decamethylcobaltocene in THF/250 mM H$_2$O to 4 mL 7 mM solution of

$[LFe_3O(Pz)_3Mn(OH)][BAr^F{}_4]$ (**6-[$BAr^F{}_4$]**; 0.03 mmol) in THF/250 mM H_2O leads to a color change of the solution from red to blue. The reaction was pumped down after 30 minutes. ^1H NMR (500 MHz, THF/C_6D_6 [250mM H_2O]): δ 126.0 (br), 76.1 (br), 59.6, 49.0, 46.9, 42.7, 37.0, 23.9 (br), 17.2, 15.6, 12.8, -14.9.

*Synthesis of $[LFe_3O(Pz)_3Mn(OH)][BAr^F{}_4]_2$ (**7-[$BAr^F{}_4$]**). Method A.* Addition of 160 μL of a 50 mM solution of Et_3N in THF/250 mM H_2O to 2 mL 2 mM solution of $[LFe_3O(Pz)_3Mn][BAr^F{}_4]_3$ (**3-[$BAr^F{}_4$]**) in THF/250 mM H_2O leads to a color change of the solution from brown to brown-green. ^1H NMR spectroscopy confirms complete conversion to $[LFe_3O(Pz)_3Mn(OH)][BAr^F{}_4]_2$.

Method B. Addition of 200 μL of 6 mM solution of Ag[BArF4] • 2 MeCN in THF/250 mM H_2O to 400 μL of a 3mM solution of $[LFe_3O(Pz)_3Mn(OH)][BAr^F{}_4]$ (**6-[$BAr^F{}_4$]**) in THF/250 mM H_2O leads to formation of a grey precipitate. Filtration of this solution yields a brown-green solution with an identical ^1H NMR obtained from Method A. ^1H NMR (500 MHz, THF/C_6D_6 [250 mM H_2O]: δ 110.2 (br), 89.1, 85.1, 70.0, 67.2, 62.0, 19.1 (br), 15.7, 13.1, 9.8 (br), 8.6 (br), 6.2 (br), 1.1, 0.7, 0. UV-Vis (THF/250 mM H_2O) [ε (M^{-1} cm^{-1})] 389 nm (5.29×10^3).

ELECTROCHEMICAL DETAILS

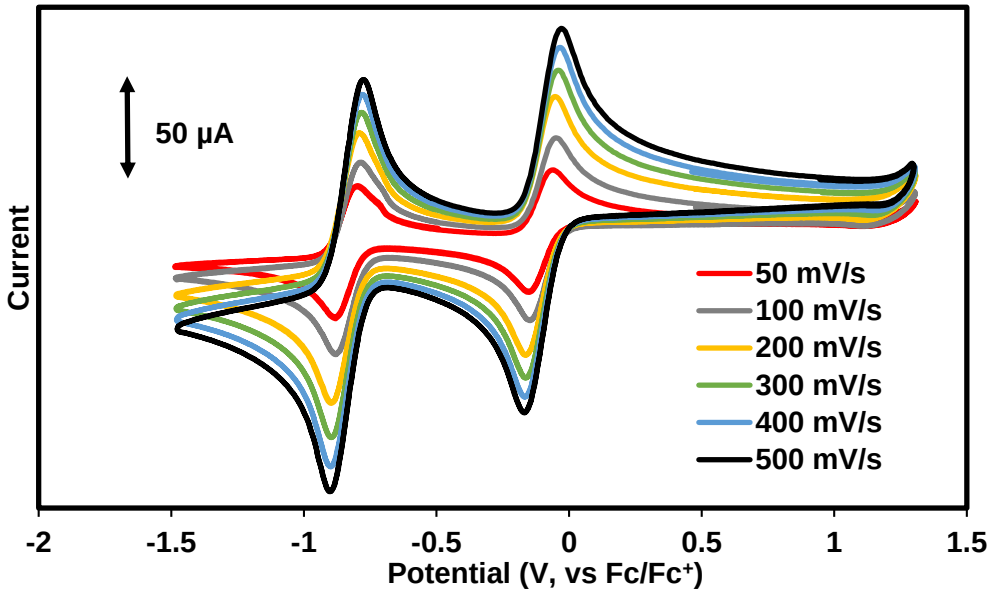

Figure 17. Cyclic voltammograms of $[LFe_3O(Pz)_3Mn][OTf]_2$ (**2-[OTf]**, 2.8 mM) in MeCN and 100 mM $[Bu_4N][PF_6]$ at various scan rates with glassy carbon, Pt-wire, and Ag-wire as working, counter, and reference electrode, respectively.

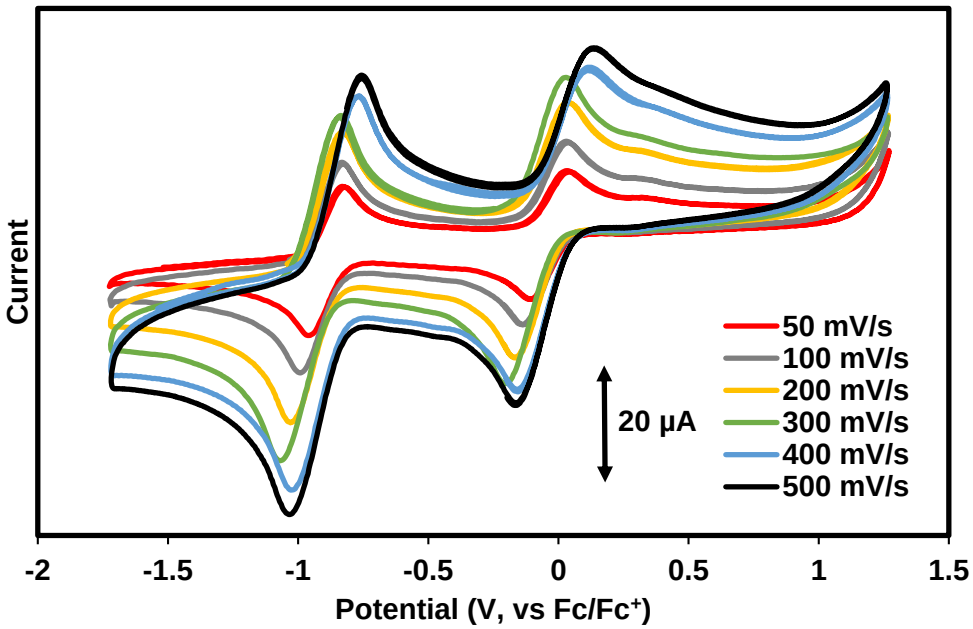

Figure 18. Cyclic voltammograms of $[LFe_3O(Pz)_3Mn(OH_2)][BAr^F{}_4]_2$ (**2-[BAr$^F{}_4$]**, 2.1 mM) in THF [250 mM H_2O] and 100 mM $[^nPr_4N][BAr^F{}_4]$ at various scan rates with glassy carbon, Pt-wire, and Ag-wire as working, counter, and reference electrode, respectively.

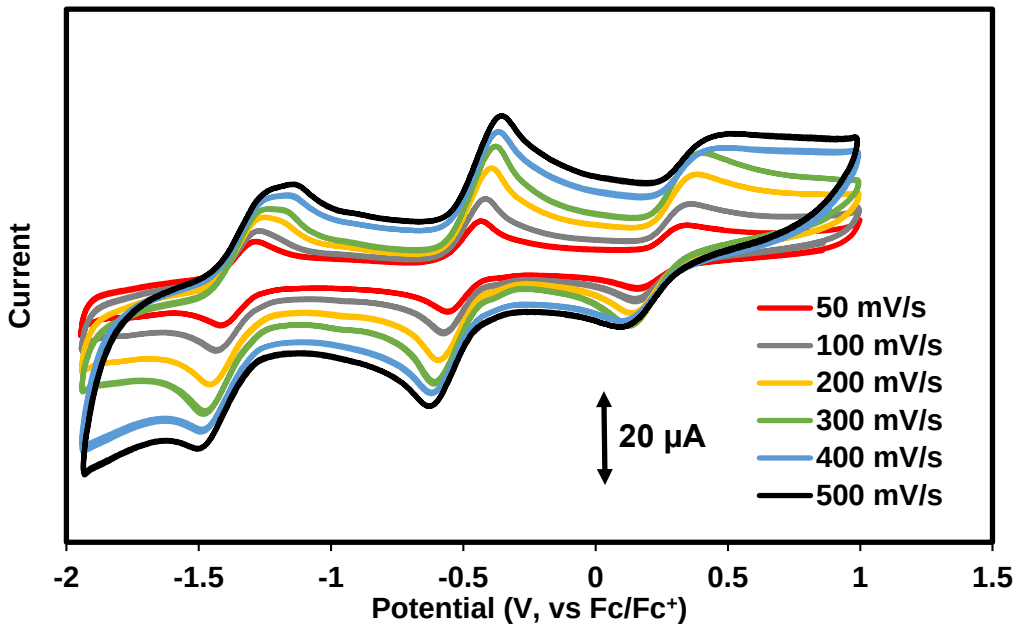

Figure 19. Cyclic voltammograms of $[LFe_3O(Pz)_3Mn(OH)][BAr^F{}_4]$ (**6-[BAr$^F{}_4$]**, 2 mM) in THF [250 mM H_2O] and 100 mM $[^nPr_4N][BAr^F{}_4]$ at various scan rates with glassy carbon, Pt-wire, and Ag-wire as working, counter, and reference electrode, respectively.

Table 3. Peak-to-peak separation (ΔE_p; mV) and peak area ratio ($A_{a/c}$) for the redox couples in 2-[OTf], 2-[BAr$^F{}_4$], and 6-[BAr$^F{}_4$].

Redox Couple Assignment	E_{pa} (mV)	E_{pc}(mV)	ΔE_p(mV)	A_a (µW)	A_c (µW)	A_a/A_p
2-[OTf]						
$[Fe^{II}_2Fe^{III}Mn^{II}] \rightarrow [Fe^{II}Fe^{III}_2Mn^{II}]$	-882	-799	83	22.0	18.5	1.2
$[Fe^{II}Fe^{III}_2Mn^{II}] \rightarrow [Fe^{III}_3Mn^{II}]$	-154	-66	88	11.4	12.2	0.9
2-[BAr$^F{}_4$]						
$[Fe^{II}_2Fe^{III}Mn^{II}] \rightarrow [Fe^{II}Fe^{III}_2Mn^{II}]$	-958	-831	127	7.9	2.8	2.8
$[Fe^{II}Fe^{III}_2Mn^{II}] \rightarrow [Fe^{III}_3Mn^{II}]$	-93	44	137	2.6	2.5	1.0
6-[BAr$^F{}_4$]						
$[Fe^{II}_3Mn^{III}] \rightarrow [Fe^{II}_2Fe^{III}Mn^{III}]$	-1,406	-1,274	132	6.6	2.6	2.5
$[Fe^{II}_2Fe^{III}Mn^{III}] \rightarrow [Fe^{II}Fe^{III}_2Mn^{III}]$	-548	-426	122	4.2	3.6	1.2
$[Fe^{II}Fe^{III}_2Mn^{III}] \rightarrow [Fe^{III}_3Mn^{III}]$	172	354	182	1.6	3.0	0.5

Constructing the Potential – pK_a Diagram of [$LFe_3O(Pz)_3Mn(OH_x)$] Clusters. Cyclic voltammetry was performed on ~2 mM solutions of $[LFe_3O(Pz)_3Mn][BAr^F{}_4]_2$ (**2-[$BAr^F{}_4$]**), or $[LFe_3O(Pz)_3Mn(OH)][BAr^F{}_4]$ (**6-[$BAr^F{}_4$]**) with glassy carbon working, Pt wire counter, and Ag wire reference electrodes in THF [250 mM H_2O] and ca. 100 mM $[^nPr_4N][BAr^F{}_4]$. After collecting a blank CV, and CV of the cluster, one equivalent of a base was added by injecting a concentrated solution of it to the cluster solution and mixing via pipette. It was observed that quasi-reversible waves corresponding to PCET could be observed best at slow scan rates (< 200 mV/s) for all bases tested; faster scan rates led to loss of a return wave for the PCET. We postulate that proton transfer in these experiments is slow relative to the time scale of electrochemistry. With some bases, redox events for the PCET and fully protonated/deprotonated cluster could be observed simultaneously; we propose that this is due to a lower local concentration of base at the electrode surface, or slow proton transfer kinetics. For all measurements reported, it is assumed that half an equivalent of available base is consumed at the electrode at the PCET $E_{½}$ potential; making the observed potential based only on the redox potential of the Mn–OH_x cluster, and the pK_a of the added base.[29] All THF pK_a values used here were obtained from a report by Rosés and co-workers.[22]

Base with **2-[BAr$^F_4$]**	pK_a (THF)	$E_{½}(1)$ (V)	$E_{½}(2)$ (V)	$E_{½}(3)$ (V)
2-methyl-aniline	7.5	-0.885	-0.002 (-0.266)	
2-methyl-pyridine	8.6	-0.891	-0.028	0.327
2,6-dimethyl-pyridine	9.5	-0.894	-0.082	
2,4,6-trimethyl-pyridine	10.4	-0.907	-0.390	
triethylamine	14.9	-0.900	-0.373	
2-phenyl-1,1,3,3-tetramethylguanidine	16.5	-0.956	-0.468	
1,1,3,3-tetramethylguanidine	17.8	-1.034	-0.454	
1,8-diazabicyclo[5.4.0]undec-7-ene	19.1	-1.066	-0.468	
7-methyl-1,5,7-triazabicyclo[4.4.0]dec-5-ene	20.5	-1.148	-0.460	
1,5,7-triazabicyclo[4.4.0]dec-5-ene	22.0	-1.180	-0.451	
tert-butylimino-tri(pyrrolidino)phosphorane	22.8	-1.271	-0.461	
1-ethyl-2,2,4,4,4-pentakis(dimethylamino)2-λ^5,4λ^5-catenadi(phosphazene)	28.1	-1.317	-0.453	
Base with **6-[BAr$^F_4$]**				
tert-butylimino-tri(pyrrolidino)phosphorane	22.8	-1.307	-0.517	0.245
1-ethyl-2,2,4,4,4-pentakis(dimethylamino)2-λ^5,4λ^5-catenadi(phosphazene)	28.1	-1.333	-0.449	0.403

All reported potentials referenced to Fc/Fc$^+$.

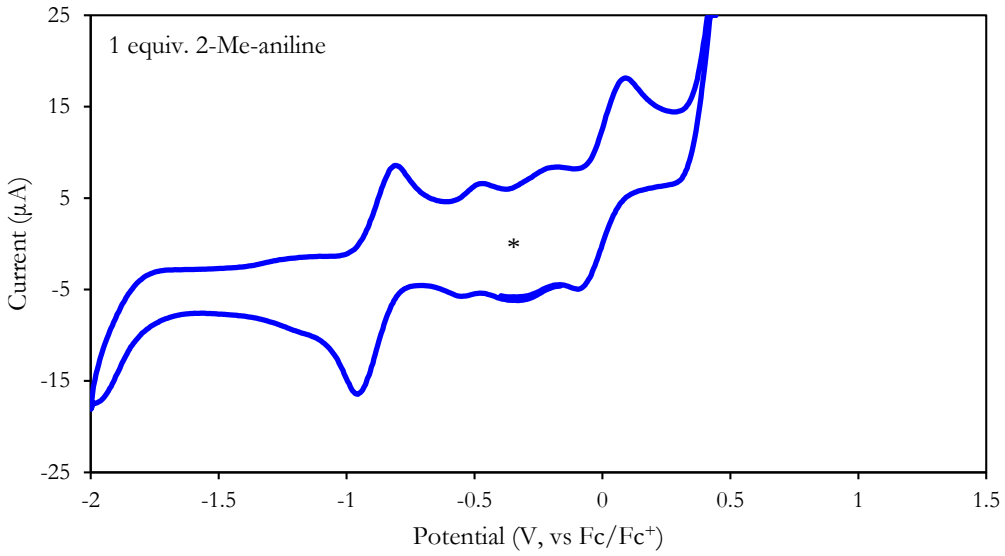

Figure 20. Cyclic voltammogram of [LFe$_3$O(Pz)$_3$Mn][BAr$^F_4$]$_2$ (**2-[BAr$^F_4$]**, 2 mM) in THF [250 mM H_2O] and 100 mM [^{n}Pr$_4$N][BAr$^F_4$] upon addition of 1 equivalent 2-methyl-aniline (pK_a(THF) = 7.5) at a scan rate of 50 mV/s. Asterisk (*) denotes redox couple of the decamethylferrocene internal standard. The open circuit potential was -0.4 V.

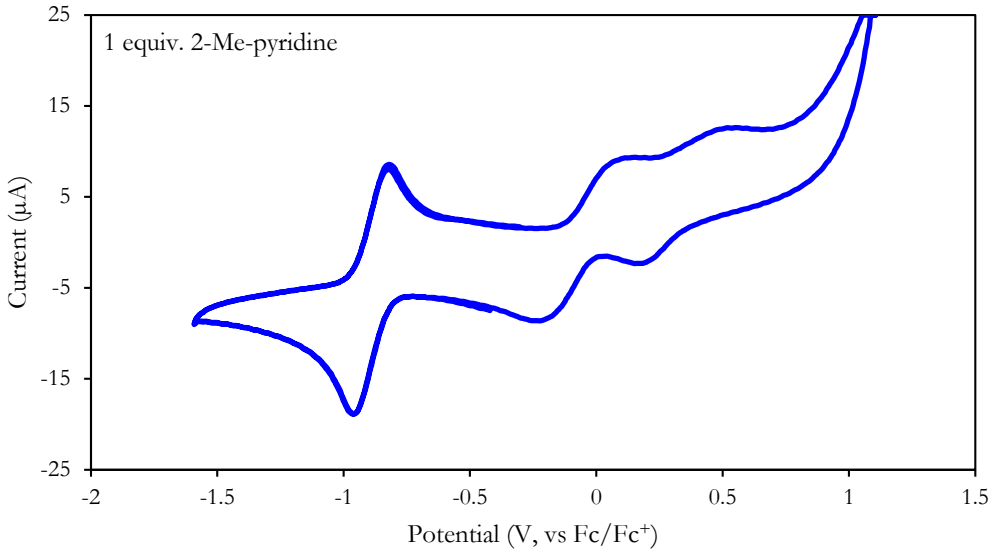

Figure 21. Cyclic voltammogram of $[LFe_3O(Pz)_3Mn][BAr^F{}_4]_2$ (**2-[BAr$^F{}_4$]**, 2 mM) in THF [250 mM H_2O] and 100 mM $[^nPr_4N][BAr^F{}_4]$ upon addition of 1 equivalent 2-methyl-pyridine (pK_a(THF) = 8.6) at a scan rate of 50 mV/s. An independent scan in the presence of a decamethylferrocene internal standard was used as a reference. The open circuit potential was -0.3 V.

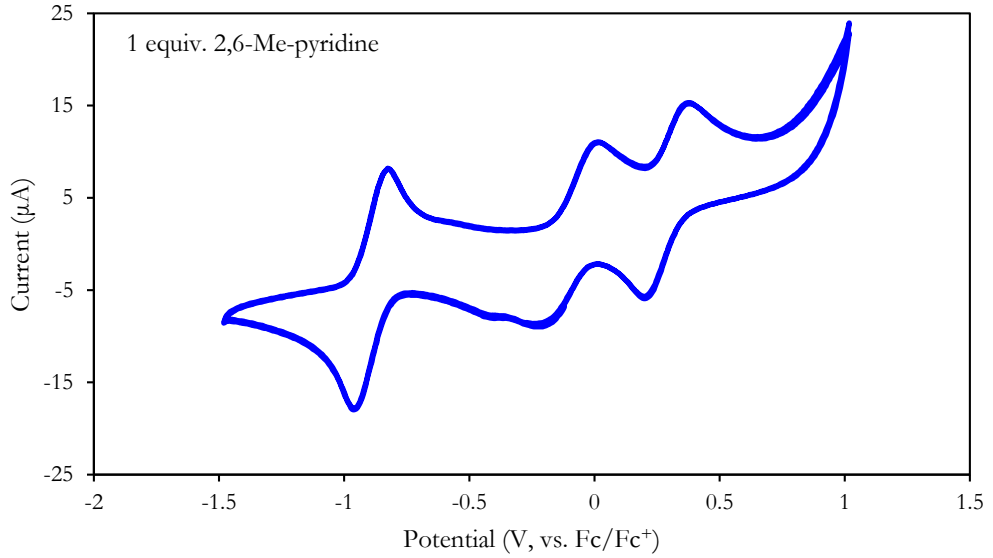

Figure 22. Cyclic voltammogram of $[LFe_3O(Pz)_3Mn][BAr^F{}_4]_2$ (**2-[BAr$^F{}_4$]**, 2 mM) in THF [250 mM H_2O] and 100 mM $[^nPr_4N][BAr^F{}_4]$ upon addition of 1 equivalent 2,6-dimethyl-pyridine

(pK_a(THF) = 9.5) at a scan rate of 50 mV/s. An independent scan in the presence of a decamethylferrocene internal standard was used as a reference. The open circuit potential was -0.3 V.

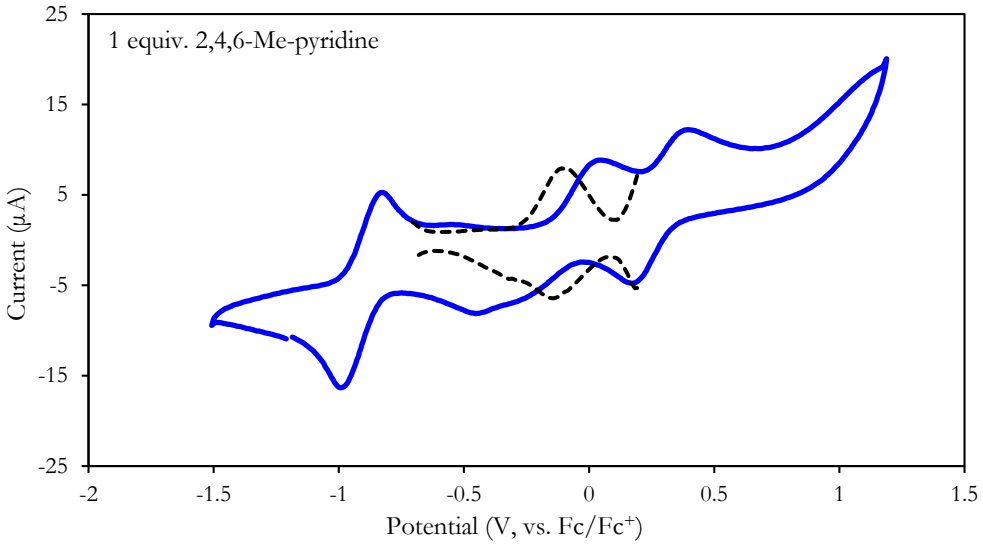

Figure 23. Cyclic voltammogram of $[LFe_3O(Pz)_3Mn][BAr^F{}_4]_2$ (**2-[BAr$^F{}_4$]**, 2 mM) in THF [250 mM H_2O] and 100 mM $[^nPr_4N][BAr^F{}_4]$ upon addition of 1 equivalent 2,4,6-trimethyl-pyridine (pK_a(THF) = 10.4) at a scan rate of 50 mV/s. An independent scan in the presence of a decamethylferrocene internal standard was used as a reference. The open circuit potential was -0.3 V. The $E_{½}$ of middle peak was determined via square wave voltammetry since its return wave was low in current, and overlapping with another peak.

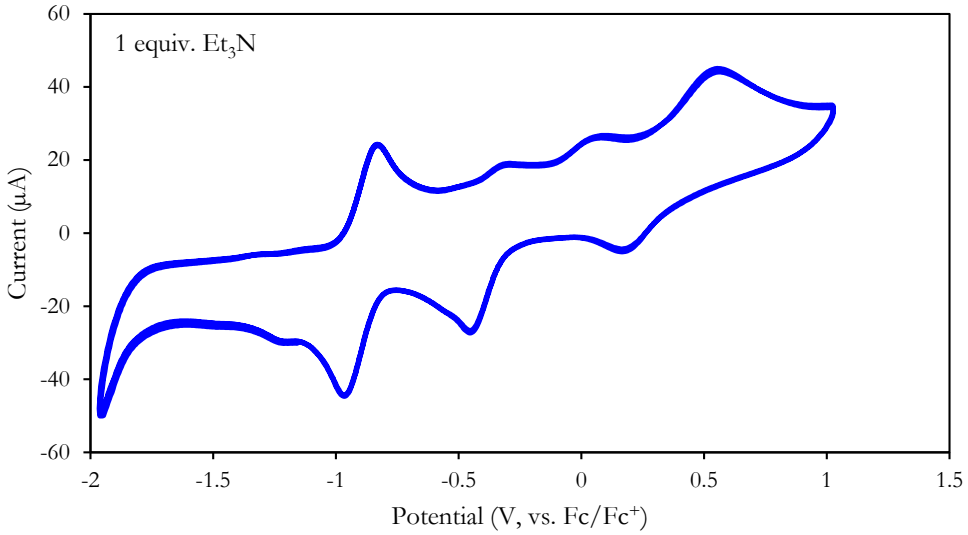

Figure 24. Cyclic voltammogram of $[LFe_3O(Pz)_3Mn][BAr^F{}_4]_2$ (**2-[BAr$^F{}_4$]**, 2 mM) in THF [250 mM H_2O] and 100 mM $[^nPr_4N][BAr^F{}_4]$ upon addition of 1 equivalent triethylamine (pK_a(THF) = 14.9) at a scan rate of 200 mV/s. An independent scan in the presence of a ferrocene internal standard was used as a reference. The open circuit potential was -0.6 V.

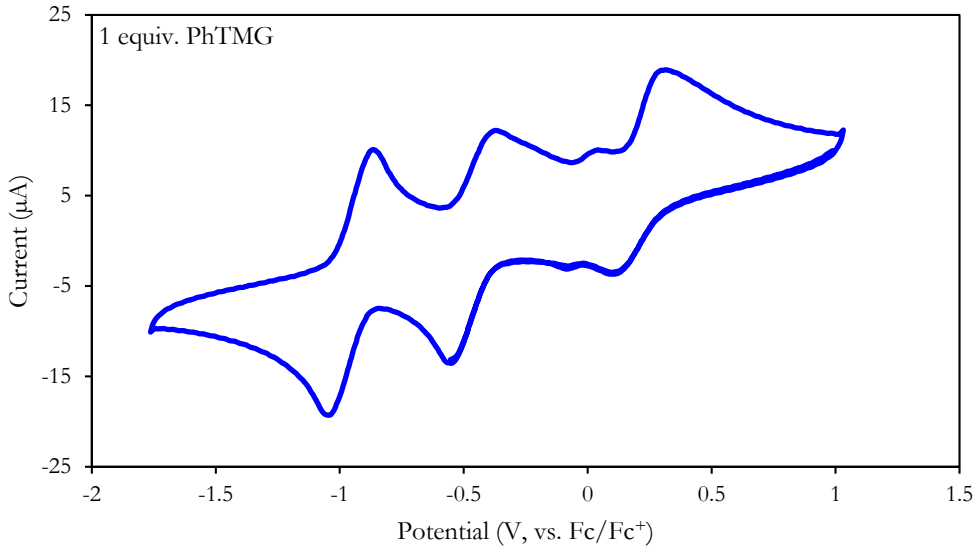

Figure 25. Cyclic voltammogram of $[LFe_3O(Pz)_3Mn][BAr^F{}_4]_2$ (**2-[BAr$^F{}_4$]**, 2 mM) in THF [250 mM H_2O] and 100 mM $[^nPr_4N][BAr^F{}_4]$ upon addition of 1 equivalent 2-phenyl-1,1,3,3-tetramethylguanidine (pK_a(THF) = 16.5) at a scan rate of 50 mV/s. An independent scan in

the presence of a ferrocene internal standard was used as a reference. The open circuit potential was -0.7 V.

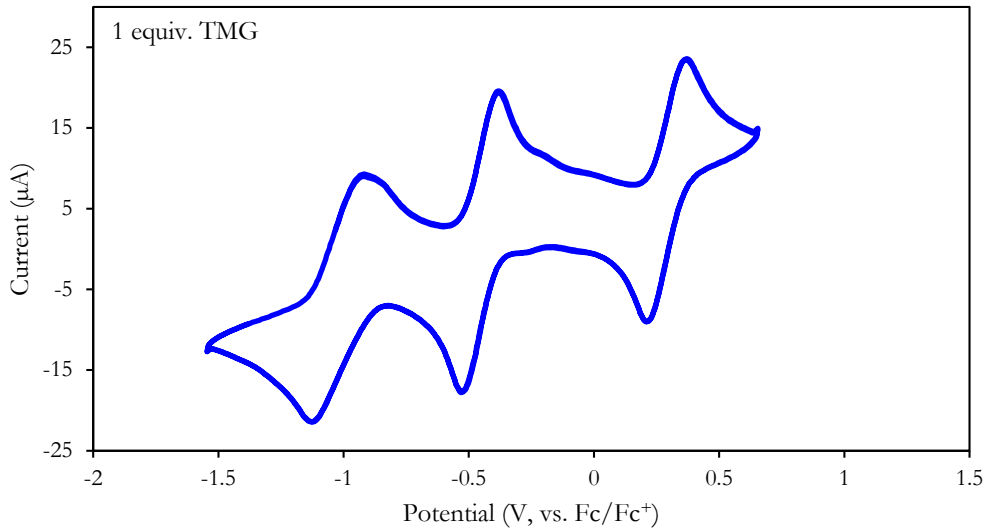

Figure 26. Cyclic voltammogram of $[LFe_3O(Pz)_3Mn][BAr^F{}_4]_2$ (**2-[BAr$^F{}_4$]**, 2 mM) in THF [250 mM H_2O] and 100 mM $[^nPr_4N][BAr^F{}_4]$ upon addition of 1 equivalent 1,1,3,3-tetramethylguanidine (pK_a(THF) = 17.8) at a scan rate of 50 mV/s. An independent scan in the presence of a ferrocene internal standard was used as a reference. The open circuit potential was -0.5 V.

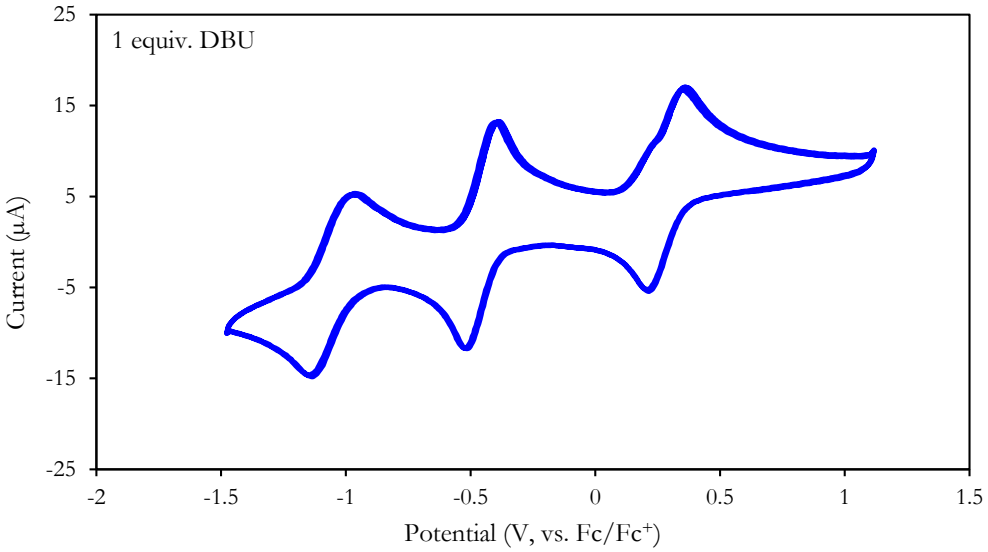

Figure 27. Cyclic voltammogram of $[LFe_3O(Pz)_3Mn][BAr^F{}_4]_2$ (**2-[BAr$^F{}_4$]**, 2 mM) in THF [250 mM H_2O] and 100 mM $[^nPr_4N][BAr^F{}_4]$ upon addition of 1 equivalent 1,8-diazabicyclo[5.4.0]undec-7-ene (pK_a(THF) = 19.1) at a scan rate of 50 mV/s. An independent scan in the presence of a ferrocene internal standard was used as a reference. The open circuit potential was -0.7 V.

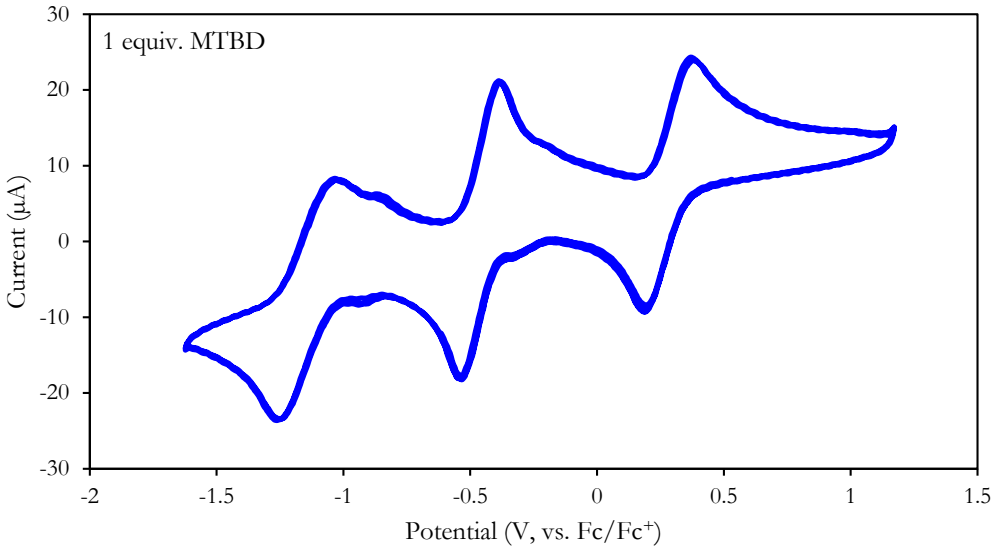

Figure 28. Cyclic voltammogram of $[LFe_3O(Pz)_3Mn][BAr^F{}_4]_2$ (**2-[BAr$^F{}_4$]**, 2 mM) in THF [250 mM H_2O] and 100 mM $[^nPr_4N][BAr^F{}_4]$ upon addition of 1 equivalent 7-methyl-1,5,7-triazabicyclo[4.4.0]dec-5-ene (pK_a(THF) = 20.5) at a scan rate of 50 mV/s. An independent scan in the presence of a ferrocene internal standard was used as a reference. The open circuit potential was -0.7 V.

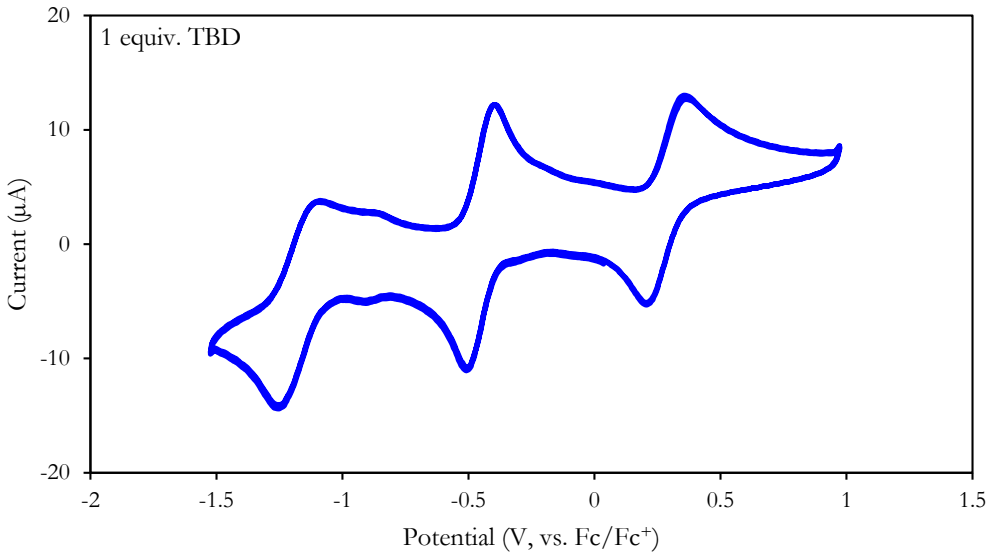

Figure 29. Cyclic voltammogram of $[LFe_3O(Pz)_3Mn][BAr^F{}_4]_2$ (**2-[BAr$^F{}_4$]**, 2 mM) in THF [250 mM H_2O] and 100 mM $[^nPr_4N][BAr^F{}_4]$ upon addition of 1 equivalent 1,5,7-triazabicyclo[4.4.0]dec-5-ene (pK_a(THF) = 22.0) at a scan rate of 50 mV/s. An independent scan in the presence of a ferrocene internal standard was used as a reference. The open circuit potential was -0.7 V.

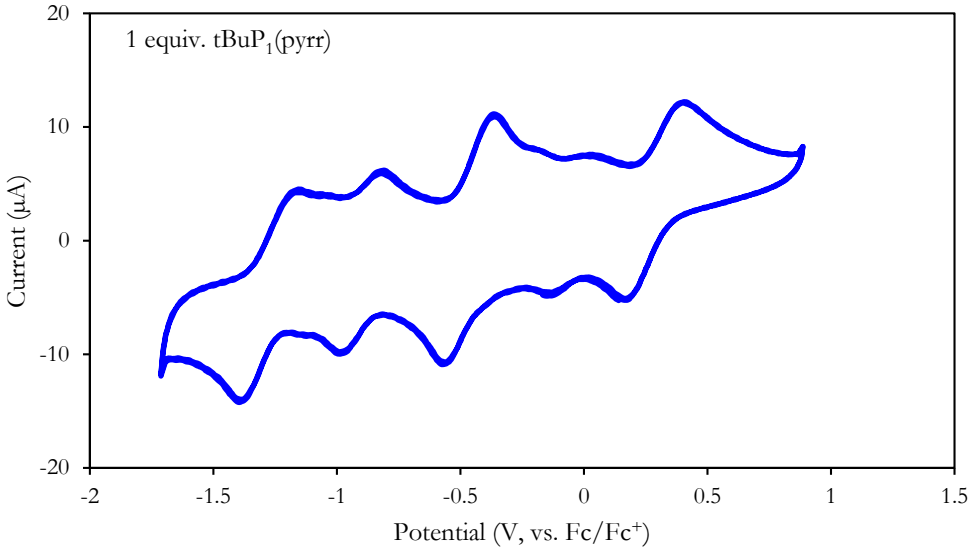

Figure 30. Cyclic voltammogram of $[LFe_3O(Pz)_3Mn][BAr^F{}_4]_2$ (**2-[BAr$^F{}_4$]**, 2 mM) in THF [250 mM H_2O] and 100 mM $[^nPr_4N][BAr^F{}_4]$ upon addition of 1 equivalent *tert*-butylimino-

tri(pyrrolidino)phosphorane (pK_a(THF) = 22.8) at a scan rate of 50 mV/s. An independent scan in the presence of a ferrocene internal standard was used as a reference. The open circuit potential was -0.7 V.

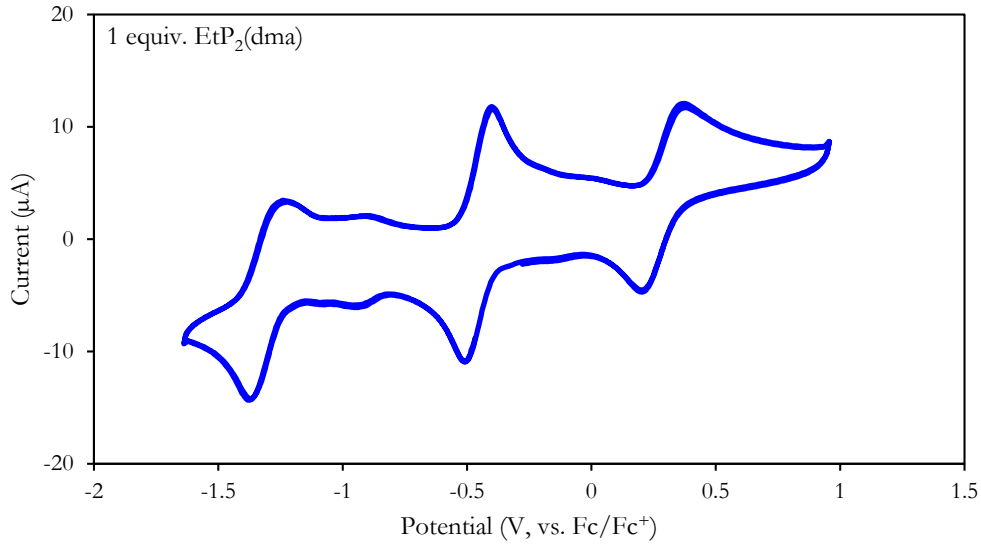

Figure 31. Cyclic voltammogram of [LFe$_3$O(Pz)$_3$Mn][BAr$^F{}_4$]$_2$ (**2-[BAr$^F{}_4$]**, 2 mM) in THF [250 mM H_2O] and 100 mM [^{n}Pr$_4$N][BAr$^F{}_4$] upon addition of 1 equivalent 1-ethyl-2,2,4,4,4-pentakis(dimethylamino)2λ^5,4λ^5-catenadi(phosphazene) (pK_a(THF) = 28.1) at a scan rate of 50 mV/s. An independent scan in the presence of a ferrocene internal standard was used as a reference. The open circuit potential was -0.7 V.

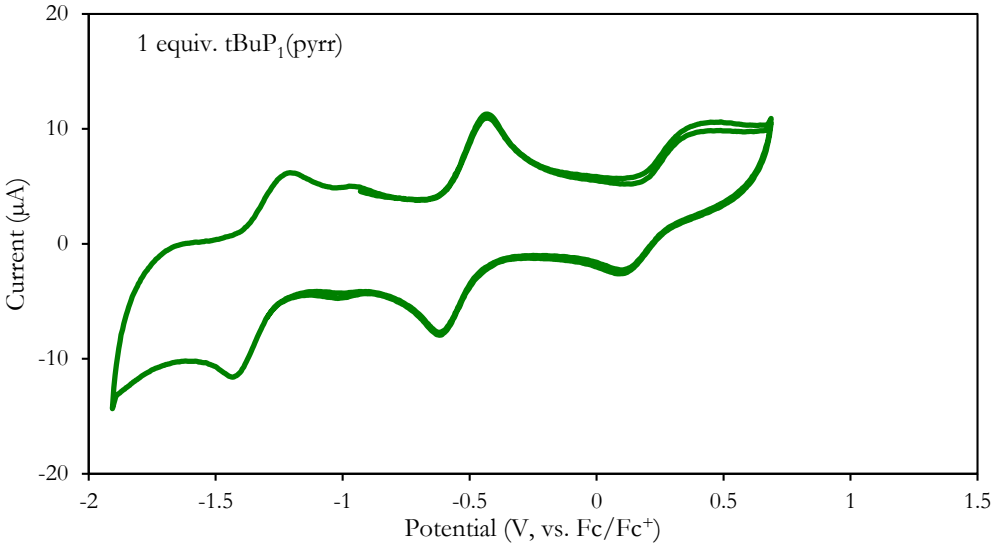

Figure 32. Cyclic voltammogram of $[LFe_3O(Pz)_3Mn(OH)][BAr^F{}_4]$ (**6-[BAr$^F{}_4$]**, 2 mM) in THF [250 mM H_2O] and 100 mM $[^nPr_4N][BAr^F{}_4]$ upon addition of 1 equivalent *tert*-butylimino-tri(pyrrolidino)phosphorane (pK_a(THF) = 22.8) at a scan rate of 50 mV/s. An independent scan in the presence of a ferrocene internal standard was used as a reference. The open circuit potential was -1.3 V.

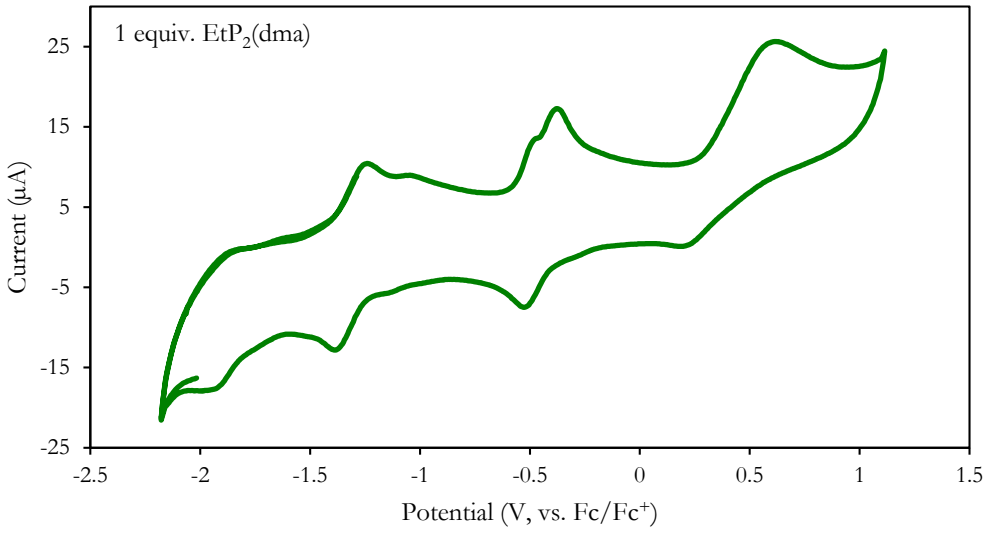

Figure 33. Cyclic voltammogram of $[LFe_3O(Pz)_3Mn(OH)][BAr^F{}_4]$ (**6-[BAr$^F{}_4$]**, 2 mM) in THF [250 mM H_2O] and 100 mM $[^nPr_4N][BAr^F{}_4]$ upon addition of 1 equivalent 1-ethyl-2,2,4,4,4-

pentakis(dimethylamino)2λ^5,4λ^5-catenadi(phosphazene) (pK_a(THF) = 28.1) at a scan rate of 50 mV/s. An independent scan in the presence of a ferrocene internal standard was used as a reference. The open circuit potential was -1.3 V.

CRYSTALOGRAPHIC DETAILS

Crystal and refinement data for complexes 1-[OTf] – 3-[OTf], 6-[OTf] and 2-[OTf] (H_2O).

	1-[OTf]	2-[OTf]	3-[OTf]	6-[OTf]	2-[OTf] (H_2O)
CCDC Number	1848679	1848681	1848680	1848678	1848677
Empirical formula	$C_{77}H_{62}F_3Fe_3MnN_{12}O_8S$	$C_{105.2}H_{81.2}BCl_{0.5}F_3Fe_3MnN_{12}O_{10.5}S$	$C_{76}H_{53.5}F_9Fe_3MnN_{13.4}O_{14.1}S_3$	$C_{67}H_{49}F_3Fe_3MnN_{12}O_8S$	$C_{72}H_{62}F_6Fe_3MnN_{12}O_{13}S_2$
Formula weight (g/mol)	1594.9	2019.8	1869.7	1461.7	1703.9
Radiation	MoKα (λ = 0.71073)	MoKα (λ = 0.71073)	CuKα (λ = 1.54178)	CuKα (λ = 1.54178)	CuKα (λ = 1.54178)
a (Å)	12.2741(5)	14.2908(12)	44.125(2)	14.7283(7)	12.2685(6)
b (Å)	19.4126(8)	15.9691(13)	14.3106(7)	19.3808(10)	29.896(2)
c (Å)	15.5112(6)	24.3709(17)	24.8034(10)	45.518(2)	19.6152(17)
α (°)	90	71.236(4)	90	90	90
β (°)	108.397(2)	75.366(2)	90.402(3)	92.474(3)	92.393(5)
γ (°)	90	70.262(4)	90	90	90
V (Å^3)	3507.0(2)	4891.6(7)	15661.9(13)	12980.9(11)	7188.2(9)
Z	2	2	8	8	4
Cryst. syst.	monoclinic	triclinic	monoclinic	monoclinic	monoclinic
Space group	$P2_1$	P-1	C2/c	C2/c	$P2_1/c$
$\varrho_{calc}g$ (cm^3)	1.510	1.371	1.586	1.496	1.575
2 Θ range (°)	5.028 to 56.648	5.076 to 60.444	6.492 to 145.272	7.544 to 132.498	5.392 to 149.51
μ (mm^{-1})	0.899	0.668	7.226	7.742	7.461
GOF	1.031	1.029	1.037	1.160	1.140
R1, wR2 (I>2σ (I))	0.0244, 0.0583	0.0635, 0.1712	0.0840, 0.2131	0.1305, 0.2771	0.1109, 0.2060

Special refinement details for [LFe$_3$O(Pz)$_3$Mn][OTf] (1-[OTf]). The triflate counterion bound to Mn1 is disordered over two positions with refined occupancies of 12% (S200 through C200) and 88% (S201 through C201).

Special refinement details for [LFe$_3$O(Pz)$_3$Mn][OTf]$_2$ (2-[OTf]). The triflate counterion bound to Mn1 is disordered over two positions with refined occupancies of 51% (S200 through C200) and 49% (S201 through C201). A disordered THF molecule was modeled over two positions with occupancies of 81% (O102 through C107) and 19% (O101 through C111). A different THF molecule was modeled to be only partially occupied (56%; O103 through C115). A co-crystallized solvent site was modeled to contain a mixture of three different molecules: a THF (27% O105 through C123), a DCM (22%; Cl10 through C124), and Et$_2$O (64%; O104 through C119).

Special refinement details for [LFe$_3$O(Pz)$_3$Mn][OTf]$_3$ (3-[OTf]). The triflate counterion bound to Mn1 is disordered over two positions with refined occupancies of 30% (S200 through C200) and 70% (S201 through C201). An outersphere triflate was modeled in two different positions with occupancies of 38% (S203 through C203) and 62% (S204 through C204). For the S203 through C203 triflate, a nearby Et$_2$O molecule was modeled as partially occupied at 62%. For the S204 through C204, a nearby MeCN molecule was modeled as partially occupied at 38%.

Special refinement details for [LFe$_3$O(Pz)$_3$Mn(OH)][OTf] (6-[OTf]).. The outersphere triflate is disordered over two positions, modeled at an occupancy of 50% each. Both triflates are on symmetry elements and positionally disordered. For the S200 through C200 triflate, this was modeled with EXYZ/EADP constraints. For the S201 throughC201 triflate, the C and S atoms were constrained with EXYZ/EACDP, and the O203 through F205 atoms were modeled in alternating positions, at 50% occupancy each. A void in the structure was a mixture

of different solvent molecules that couldn't be adequately modeled, and a solvent mask was used to account for this electron density.

References

1. (a) McEvoy, J. P.; Brudvig, G. W. *Chem. Rev.* **2006,** *106*, 4455-4483; (b) Ferreira, K. N.; Iverson, T. M.; Maghlaoui, K.; Barber, J.; Iwata, S. *Science* **2004,** *303*, 1831-1838; (c) Umena, Y.; Kawakami, K.; Shen, J.-R.; Kamiya, N. *Nature* **2011,** *473*, 55-60; (d) Suga, M.; Akita, F.; Hirata, K.; Ueno, G.; Murakami, H.; Nakajima, Y.; Shimizu, T.; Yamashita, K.; Yamamoto, M.; Ago, H.; Shen, J.-R. *Nature* **2015,** *517*, 99-103.
2. (a) Kok, B.; Forbush, B.; McGloin, M. *Photochem. Photobiol.* **1970,** *11*, 457-475; (b) Yano, J.; Yachandra, V. *Chem. Rev.* **2014,** *114*, 4175-4205; (c) Vinyard, D. J.; Brudvig, G. W. *Annu. Rev. Phys. Chem.* **2017,** *68*, 101-116.
3. Meyer, T. J.; Huynh, M. H. V.; Thorp, H. H. *Angew. Chem. Int. Ed.* **2007,** *46*, 5284-5304.
4. (a) Weinberg, D. R.; Gagliardi, C. J.; Hull, J. F.; Murphy, C. F.; Kent, C. A.; Westlake, B. C.; Paul, A.; Ess, D. H.; McCafferty, D. G.; Meyer, T. J. *Chem. Rev.* **2012,** *112*, 4016-4093; (b) Migliore, A.; Polizzi, N. F.; Therien, M. J.; Beratan, D. N. *Chem. Rev.* **2014,** *114*, 3381-3465; (c) Amin, M.; Vogt, L.; Szejgis, W.; Vassiliev, S.; Brudvig, G. W.; Bruce, D.; Gunner, M. R. *J. Phys. Chem. B* **2015,** *119*, 7366-7377.
5. Suga, M.; Akita, F.; Sugahara, M.; Kubo, M.; Nakajima, Y.; Nakane, T.; Yamashita, K.; Umena, Y.; Nakabayashi, M.; Yamane, T.; Nakano, T.; Suzuki, M.; Masuda, T.; Inoue, S.; Kimura, T.; Nomura, T.; Yonekura, S.; Yu, L.-J.; Sakamoto, T.; Motomura, T.; Chen, J.-H.; Kato, Y.; Noguchi, T.; Tono, K.; Joti, Y.; Kameshima, T.; Hatsui, T.; Nango, E.; Tanaka, R.; Naitow, H.; Matsuura, Y.; Yamashita, A.; Yamamoto, M.; Nureki, O.; Yabashi, M.; Ishikawa, T.; Iwata, S.; Shen, J.-R. *Nature* **2017,** *543*, 131-135.
6. (a) Oyala, P. H.; Stich, T. A.; Stull, J. A.; Yu, F.; Pecoraro, V. L.; Britt, R. D. *Biochemistry* **2014,** *53*, 7914-7928; (b) Sjöholm, J.; Styring, S.; Havelius, K. G. V.; Ho, F. M. *Biochemistry* **2012,** *51*, 2054-2064; (c) Asada, M.; Nagashima, H.; Koua, F. H. M.; Shen, J.-R.; Kawamori, A.; Mino, H. *BBA - Bioenergetics* **2013,** *1827*, 438-445; (d) Krewald, V.; Retegan, M.; Cox, N.; Messinger, J.; Lubitz, W.; DeBeer, S.; Neese, F.; Pantazis, D. A. *Chemical Science* **2015,** *6*, 1676-1695; (e) Pérez Navarro, M.; Ames, W. M.; Nilsson, H.; Lohmiller, T.; Pantazis, D. A.; Rapatskiy, L.; Nowaczyk, M. M.; Neese, F.; Boussac, A.; Messinger, J.; Lubitz, W.; Cox, N. *Proc. Natl. Acad. Sci.* **2013,** *110*, 15561-15566; (f) Lohmiller, T.; Krewald, V.; Sedoud, A.; Rutherford, A. W.; Neese, F.; Lubitz, W.; Pantazis, D. A.; Cox, N. *J. Am. Chem. Soc.* **2017,** *139*, 14412-14424; (g) Lohmiller, T.; Krewald, V.; Navarro, M. P.; Retegan, M.; Rapatskiy, L.; Nowaczyk, M. M.; Boussac, A.; Neese, F.; Lubitz, W.; Pantazis, D. A.; Cox, N. *Phys. Chem. Chem. Phys.* **2014,** *16*, 11877-11892; (h) Peloquin, J. M.; Campbell, K. A.; Randall, D. W.; Evanchik, M. A.; Pecoraro, V. L.; Armstrong, W. H.; Britt, R. D. *J. Am. Chem. Soc.* **2000,** *122*, 10926-10942; (i) Rapatskiy, L.; Cox, N.; Savitsky, A.; Ames, W. M.; Sander, J.; Nowaczyk, M. M.; Rögner, M.; Boussac, A.; Neese, F.; Messinger, J.; Lubitz, W. *J. Am. Chem. Soc.* **2012,** *134*, 16619-16634; (j) Pokhrel, R.; Brudvig, G. W. *Phys. Chem. Chem. Phys.* **2014,** *16*, 11812-11821; (k) Cox, N.; Retegan, M.; Neese, F.; Pantazis, D. A.; Boussac, A.; Lubitz, W. *Science* **2014,** *345*, 804-808.
7. (a) Zaharieva, I.; Chernev, P.; Berggren, G.; Anderlund, M.; Styring, S.; Dau, H.; Haumann, M. *Biochemistry* **2016,** *55*, 4197-4211; (b) Zaharieva, I.; Dau, H.; Haumann, M. *Biochemistry* **2016,** *55*, 6996-7004; (c) Petrie, S.; Stranger, R.; Pace, R. J. *Phys. Chem. Chem. Phys.* **2017,** *19*, 27682-27693; (d) Kubin, M.; Kern, J.; Gul, S.; Kroll, T.; Chatterjee, R.; Löchel, H.; Fuller, F. D.; Sierra, R. G.; Quevedo, W.; Weniger, C.; Rehanek, J.; Firsov, A.; Laksmono, H.; Weninger, C.; Alonso-Mori, R.; Nordlund, D. L.; Lassalle-Kaiser, B.; Glownia, J. M.; Krzywinski, J.; Moeller, S.; Turner, J. J.; Minitti, M. P.; Dakovski, G. L.; Koroidov, S.; Kawde, A.; Kanady, J. S.; Tsui, E. Y.; Suseno, S.; Han, Z.; Hill, E.; Taguchi, T.; Borovik, A. S.; Agapie, T.; Messinger, J.; Erko, A.; Föhlisch, A.; Bergmann, U.; Mitzner, R.; Yachandra, V. K.; Yano, J.; Wernet, P. *Structural Dynamics* **2017,** *4*, 054307.
8. (a) Rossini, E.; Knapp, E.-W. *Coord. Chem. Rev.* **2017,** *345*, 16-30; (b) Siegbahn, P. E. M. *BBA - Bioenergetics* **2013,** *1827*, 1003-1019.
9. (a) Noguchi, T. *BBA - Bioenergetics* **2015,** *1847*, 35-45; (b) Suzuki, H.; Sugiura, M.; Noguchi, T. *J. Am. Chem. Soc.* **2009,** *131*, 7849-7857; (c) Debus, R. J. *BBA - Bioenergetics* **2015,** *1847*, 19-34; (d) Kim, C. J.; Debus, R. J. *Biochemistry* **2017,** *56*, 2558-2570; (e) Polander, B. C.; Barry, B. A. *Proc. Natl. Acad. Sci.* **2012,** *109*, 6112.

10. (a) Siegbahn, P. E. M. *Phys. Chem. Chem. Phys.* **2012,** *14*, 4849-4856; (b) Ichino, T.; Yoshioka, Y. *Chem. Phys. Lett.* **2014,** *595–596*, 237-241; (c) Sproviero, E. M.; Gascón, J. A.; McEvoy, J. P.; Brudvig, G. W.; Batista, V. S. *J. Am. Chem. Soc.* **2008,** *130*, 3428-3442; (d) Yamaguchi, K.; Isobe, H.; Yamanaka, S.; Saito, T.; Kanda, K.; Shoji, M.; Umena, Y.; Kawakami, K.; Shen, J. R.; Kamiya, N.; Okumura, M. *Int. J. Quantum Chem* **2013,** *113*, 525-541.
11. (a) Massie, A. A.; Denler, M. C.; Cardoso, L. T.; Walker, A. N.; Hossain, M. K.; Day, V. W.; Nordlander, E.; Jackson, T. A. *Angew. Chem. Int. Ed.* **2017,** *56*, 4178-4182; (b) Wijeratne, G. B.; Corzine, B.; Day, V. W.; Jackson, T. A. *Inorg. Chem.* **2014,** *53*, 7622-7634; (c) Yin, G.; Danby, A. M.; Kitko, D.; Carter, J. D.; Scheper, W. M.; Busch, D. H. *J. Am. Chem. Soc.* **2008,** *130*, 16245-16253; (d) Kurahashi, T.; Kikuchi, A.; Shiro, Y.; Hada, M.; Fujii, H. *Inorg. Chem.* **2010,** *49*, 6664-6672; (e) Hong, S.; Lee, Y.-M.; Sankaralingam, M.; Vardhaman, A. K.; Park, Y. J.; Cho, K.-B.; Ogura, T.; Sarangi, R.; Fukuzumi, S.; Nam, W. *J. Am. Chem. Soc.* **2016,** *138*, 8523-8532; (f) Chen, J.; Cho, K.-B.; Lee, Y.-M.; Kwon, Y. H.; Nam, W. *Chem. Commun.* **2015,** *51*, 13094-13097; (g) Chen, J.; Lee, Y.-M.; Davis, K. M.; Wu, X.; Seo, M. S.; Cho, K.-B.; Yoon, H.; Park, Y. J.; Fukuzumi, S.; Pushkar, Y. N.; Nam, W. *J. Am. Chem. Soc.* **2013,** *135*, 6388-6391; (h) Chen, J.; Yoon, H.; Lee, Y.-M.; Seo, M. S.; Sarangi, R.; Fukuzumi, S.; Nam, W. *Chemical Science* **2015,** *6*, 3624-3632; (i) Barman, P.; Vardhaman, A. K.; Martin, B.; Wörner, S. J.; Sastri, C. V.; Comba, P. *Angew. Chem. Int. Ed.* **2015,** *54*, 2095-2099; (j) Yin, G. *Acc. Chem. Res.* **2013,** *46*, 483-492.
12. (a) Parsell, T. H.; Yang, M.-Y.; Borovik, A. S. *J. Am. Chem. Soc.* **2009,** *131*, 2762-2763; (b) Gupta, R.; MacBeth, C. E.; Young, V. G.; Borovik, A. S. *J. Am. Chem. Soc.* **2002,** *124*, 1136-1137; (c) Gupta, R.; Borovik, A. S. *J. Am. Chem. Soc.* **2003,** *125*, 13234-13242; (d) Taguchi, T.; Stone, K. L.; Gupta, R.; Kaiser-Lassalle, B.; Yano, J.; Hendrich, M. P.; Borovik, A. S. *Chemical Science* **2014,** *5*, 3064-3071; (e) Goldsmith, C. R.; Cole, A. P.; Stack, T. D. P. *J. Am. Chem. Soc.* **2005,** *127*, 9904-9912; (f) Coggins, M. K.; Brines, L. M.; Kovacs, J. A. *Inorg. Chem.* **2013,** *52*, 12383-12393; (g) Yin, G.; Danby, A. M.; Kitko, D.; Carter, J. D.; Scheper, W. M.; Busch, D. H. *J. Am. Chem. Soc.* **2007,** *129*, 1512-1513; (h) Gardner, K. A.; Kuehnert, L. L.; Mayer, J. M. *Inorg. Chem.* **1997,** *36*, 2069-2078; (i) Lassalle-Kaiser, B.; Hureau, C.; Pantazis, D. A.; Pushkar, Y.; Guillot, R.; Yachandra, V. K.; Yano, J.; Neese, F.; Anxolabehere-Mallart, E. *Energy & Environmental Science* **2010,** *3*, 924-938; (j) Wang, Y.; Sheng, J.; Shi, S.; Zhu, D.; Yin, G. *The Journal of Physical Chemistry C* **2012,** *116*, 13231-13239; (k) Baglia, R. A.; Prokop-Prigge, K. A.; Neu, H. M.; Siegler, M. A.; Goldberg, D. P. *J. Am. Chem. Soc.* **2015,** *137*, 10874-10877.
13. (a) Gupta, R.; Taguchi, T.; Lassalle-Kaiser, B.; Bominaar, E. L.; Yano, J.; Hendrich, M. P.; Borovik, A. S. *Proc. Natl. Acad. Sci.* **2015,** *112*, 5319-5324; (b) Leto, D. F.; Massie, A. A.; Rice, D. B.; Jackson, T. A. *J. Am. Chem. Soc.* **2016,** *138*, 15413-15424; (c) Leto, D. F.; Ingram, R.; Day, V. W.; Jackson, T. A. *Chem. Commun.* **2013,** *49*, 5378-5380; (d) Yin, G.; McCormick, J. M.; Buchalova, M.; Danby, A. M.; Rodgers, K.; Day, V. W.; Smith, K.; Perkins, C. M.; Kitko, D.; Carter, J. D.; Scheper, W. M.; Busch, D. H. *Inorg. Chem.* **2006,** *45*, 8052-8061; (e) Park, Y. J.; Matson, E. M.; Nilges, M. J.; Fout, A. R. *Chem. Commun.* **2015,** *51*, 5310-5313.
14. (a) Wang, K.; Mayer, J. M. *J. Am. Chem. Soc.* **1997,** *119*, 1470-1471; (b) Baldwin, M. J.; Pecoraro, V. L. *J. Am. Chem. Soc.* **1996,** *118*, 11325-11326; (c) Sankaralingam, M.; Jeon, S. H.; Lee, Y.-M.; Seo, M. S.; Ohkubo, K.; Fukuzumi, S.; Nam, W. *Dalton Transactions* **2016,** *45*, 376-383; (d) Carrell, T. G.; Bourles, E.; Lin, M.; Dismukes, G. C. *Inorg. Chem.* **2003,** *42*, 2849-2858; (e) Thorp, H. H.; Sarneski, J. E.; Brudvig, G. W.; Crabtree, R. H. *J. Am. Chem. Soc.* **1989,** *111*, 9249-9250; (f) Amin, M.; Vogt, L.; Vassiliev, S.; Rivalta, I.; Sultan, M. M.; Bruce, D.; Brudvig, G. W.; Batista, V. S.; Gunner, M. R. *J. Phys. Chem. B* **2013,** *117*, 6217-6226.
15. (a) Caudle, M. T.; Pecoraro, V. L. *J. Am. Chem. Soc.* **1997,** *119*, 3415-3416; (b) Cady, C. W.; Shinopoulos, K. E.; Crabtree, R. H.; Brudvig, G. W. *Dalton Transactions* **2010,** *39*, 3985-3989.
16. Tsui, E. Y.; Kanady, J. S.; Agapie, T. *Inorg. Chem.* **2013,** *52*, 13833-13848.
17. (a) Herbert, D. E.; Lionetti, D.; Rittle, J.; Agapie, T. *J. Am. Chem. Soc.* **2013,** *135*, 19075-19078; (b) Tsui, E. Y.; Tran, R.; Yano, J.; Agapie, T. *Nature Chemistry* **2013,** *5*, 293-299; (c) Tsui, E. Y.; Agapie, T. *Proc. Natl. Acad. Sci.* **2013,** *110*, 10084-10088; (d) Kanady, J. S.; Tsui, E. Y.; Day, M. W.; Agapie, T. *Science* **2011,** *333*, 733-736; (e) Lin, P.-H.; Takase, M. K.; Agapie, T. *Inorg. Chem.* **2015,** *54*, 59-64.

18. (a) de Ruiter, G.; Thompson, N. B.; Lionetti, D.; Agapie, T. *J. Am. Chem. Soc.* **2015,** *137*, 14094-14106; (b) Reed, C. J.; Agapie, T. *Inorg. Chem.* **2017,** *56*, 13360-13367; (c) Arnett, C. H.; Chalkley, M. J.; Agapie, T. *J. Am. Chem. Soc.* **2018,** *140*, 5569-5578; (d) de Ruiter, G.; Thompson, N. B.; Takase, M. K.; Agapie, T. *J. Am. Chem. Soc.* **2016,** *138*, 1486-1489; (e) de Ruiter, G.; Carsch, K. M.; Gul, S.; Chatterjee, R.; Thompson, N. B.; Takase, M. K.; Yano, J.; Agapie, T. *Angew. Chem. Int. Ed.* **2017,** *56*, 4772-4776; (f) Carsch, K. M.; de Ruiter, G.; Agapie, T. *Inorg. Chem.* **2017,** *56*, 9044-9054.
19. Han, Z.; Horak, K. T.; Lee, H. B.; Agapie, T. *J. Am. Chem. Soc.* **2017,** *139*, 9108-9111.
20. Lionetti, D. Heterometallic Complexes as Models of Enzymatic Active Sites. PhD dissertation, California Institute of Technology, Pasadena, California, 2015.
21. (a) Sivanesan, D.; Kannan, S.; Thangadurai, T. D.; Jung, K.-D.; Yoon, S. *Dalton Transactions* **2014,** *43*, 11465-11469; (b) Chen, L.-Z.; Huang, D.-D.; Ge, J.-Z.; Pan, Q.-J. *J. Mol. Struct.* **2014,** *1072*, 307-312; (c) Rich, J.; Rodriguez, M.; Romero, I.; Vaquer, L.; Sala, X.; Llobet, A.; Corbella, M.; Collomb, M.-N.; Fontrodona, X. *Dalton Transactions* **2009**, 8117-8126.
22. Garrido, G.; Koort, E.; Ràfols, C.; Bosch, E.; Rodima, T.; Leito, I.; Rosés, M. *The Journal of Organic Chemistry* **2006,** *71*, 9062-9067.
23. (a) MacBeth, C. E.; Gupta, R.; Mitchell-Koch, K. R.; Young, V. G.; Lushington, G. H.; Thompson, W. H.; Hendrich, M. P.; Borovik, A. S. *J. Am. Chem. Soc.* **2004,** *126*, 2556-2567; (b) Shirin, Z.; Hammes, B. S.; Young, V. G.; Borovik, A. S. *J. Am. Chem. Soc.* **2000,** *122*, 1836-1837; (c) Shirin, Z.; S. Borovik, A.; G. Young Jr, V. *Chem. Commun.* **1997**, 1967-1968; (d) Shook, R. L.; Peterson, S. M.; Greaves, J.; Moore, C.; Rheingold, A. L.; Borovik, A. S. *J. Am. Chem. Soc.* **2011,** *133*, 5810-5817; (e) Lacy, D. C.; Mukherjee, J.; Lucas, R. L.; Day, V. W.; Borovik, A. S. *Polyhedron* **2013,** *52*, 261-267.
24. (a) Baglia, R. A.; Krest, C. M.; Yang, T.; Leeladee, P.; Goldberg, D. P. *Inorg. Chem.* **2016,** *55*, 10800-10809; (b) Leeladee, P.; Baglia, R. A.; Prokop, K. A.; Latifi, R.; de Visser, S. P.; Goldberg, D. P. *J. Am. Chem. Soc.* **2012,** *134*, 10397-10400; (c) Bougher, C. J.; Liu, S.; Hicks, S. D.; Abu-Omar, M. M. *J. Am. Chem. Soc.* **2015,** *137*, 14481-14487.
25. (a) Cappellani, E. P.; Drouin, S. D.; Jia, G.; Maltby, P. A.; Morris, R. H.; Schweitzer, C. T. *J. Am. Chem. Soc.* **1994,** *116*, 3375-3388; (b) Tilset, M. The Thermodynamics of Organometallic Systems Involving Electron-Transfer Paths. In *Electron Transfer in Chemistry, 1*, Balzani, V., Ed. Wiley-VCH: Weinheim, Germany, 2001; pp 677-713.
26. (a) Bordwell, F. G.; Satish, A. V.; Zhang, S.; Zhang, X. M. Using thermodynamic cycles to study reactive intermediates. In *Pure Appl. Chem.*, 1995; Vol. 67, p 735; (b) Mayer, J. M. *Acc. Chem. Res.* **1998,** *31*, 441-450; (c) Warren, J. J.; Tronic, T. A.; Mayer, J. M. *Chem. Rev.* **2010,** *110*, 6961-7001.
27. (a) Pourbaix, M. *Atlas of Electrochemical Equilibria in Aqueous Solutions*. 1st English ed.; Pergamon Press: Oxford, New York, 1966; (b) Slattery, S. J.; Blaho, J. K.; Lehnes, J.; Goldsby, K. A. *Coord. Chem. Rev.* **1998,** *174*, 391-416.
28. (a) Bozoglian, F.; Romain, S.; Ertem, M. Z.; Todorova, T. K.; Sens, C.; Mola, J.; Rodríguez, M.; Romero, I.; Benet-Buchholz, J.; Fontrodona, X.; Cramer, C. J.; Gagliardi, L.; Llobet, A. *J. Am. Chem. Soc.* **2009,** *131*, 15176-15187; (b) Nunes, G. S.; Alexiou, A. D. P.; Araki, K.; Formiga, A. L. B.; Rocha, R. C.; Toma, H. E. *Eur. J. Inorg. Chem.* **2006,** *2006*, 1487-1495; (c) Gilbert, J. A.; Eggleston, D. S.; Murphy, W. R.; Geselowitz, D. A.; Gersten, S. W.; Hodgson, D. J.; Meyer, T. J. *J. Am. Chem. Soc.* **1985,** *107*, 3855-3864; (d) Isobe, H.; Tanaka, K.; Shen, J.-R.; Yamaguchi, K. *Inorg. Chem.* **2014,** *53*, 3973-3984.
29. McCarthy, B. D.; Dempsey, J. L. *Inorg. Chem.* **2017,** *56*, 1225-1231.
30. The redox couple that would be assigned to the 7-[BArF] to 8-[BArF] reduction potential unexpectedly increases, inconsistent with PCET to Mn=O and may suggest an undesirable side reaction takes place at these potentials with the base employed.
31. Attempts to obtain supporting data via stoichiometric deprotonation of 7-[BArF4] with various bases led to decomposition via reduction, with no evidence of forming a transient Mn=O moiety. Investigations into the characterization and reactivity of these putative M=O species (M = Fe, Mn) in these and related clusters is ongoing.
32. Riedel, P. J.; Arulsamy, N.; Mehn, M. P. *Inorg. Chem. Commun.* **2011,** *14*, 734-737.
33. Izod, K.; Rayner, D. G.; El-Hamruni, S. M.; Harrington, R. W.; Baisch, U. *Angew. Chem. Int. Ed.* **2014,** *53*, 3636-3640.

34. Huang, C.-Y.; Doyle, A. G. *J. Am. Chem. Soc.* **2012,** *134*, 9541-9544.
35. Zhang, Y.; Santos, A. M.; Herdtweck, E.; Mink, J.; Kuhn, F. E. *New J. Chem.* **2005,** *29*, 366-370.
36. Manner, V. W.; Markle, T. F.; Freudenthal, J. H.; Roth, J. P.; Mayer, J. M. *Chem. Commun.* **2008**, 256-258.
37. Thomson, R. K.; Scott, B. L.; Morris, D. E.; Kiplinger, J. L. *Comptes Rendus Chimie* **2010,** *13*, 790-802.
38. (a) Herold, S.; Lippard, S. J. *Inorg. Chem.* **1997,** *36*, 50-58; (b) Singh, A. K.; Jacob, W.; Boudalis, A. K.; Tuchagues, J.-P.; Mukherjee, R. *Eur. J. Inorg. Chem.* **2008,** *2008*, 2820-2829; (c) Sutradhar, M.; Carrella, L. M.; Rentschler, E. *Eur. J. Inorg. Chem.* **2012,** *2012*, 4273-4278; (d) Schünemann, V.; Hauke, P. Mössbauer Spectroscopy. In *Applications of Physical Methods to Inorganic and Bioinorganic Chemistry*, Scott, R. A.; Lukehart, C. M., Eds. John Wiley & Sons: West Sussex, England, 2007; pp 243-269.